Cell

Molecular architecture of human dermal sleeping nociceptors

Graphical abstract

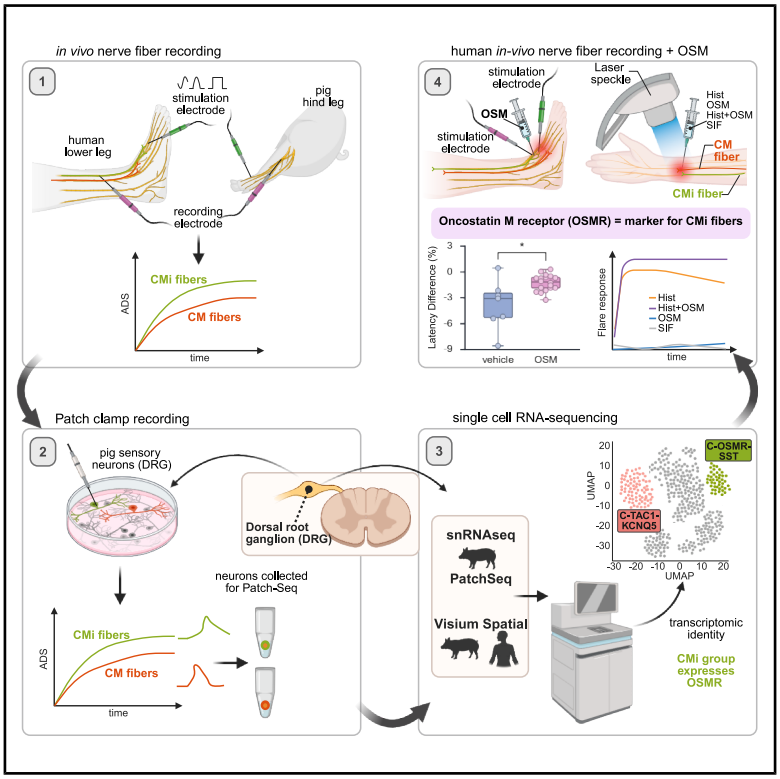

Highlights

- Human dermal mechano-insensitive CMi-fiber activity is linked to neuropathic pain
- Patch-seq maps CMi electrophysiology to single-cell transcriptomes
- OSMR and SST are molecular markers of human CMi nociceptors
- CMi molecular architecture suggests targets for neuropathic pain therapy

Authors

Jannis Körner, Derek Howard, Hans Jürgen Solinski, ..., Barbara Namer, Shreejoy Tripathy, Angelika Lampert

Correspondence

shreejoy.tripathy@camh.ca (S.T.), alampert@ukaachen.de (A.L.)

In brief

Integration of electrophysiology with single-cell transcriptomics defines the molecular signature of human dermal sleeping nociceptors and reveals oncostatin M as a selective modulator of these neurons in humans, providing a therapeutic entry point for neuropathic pain.

Körner et al., 2026, Cell *189*, 1820–1835
March 19, 2026 © 2025 The Authors. Published by Elsevier Inc.
https://doi.org/10.1016/j.cell.2025.12.048

CellPress

CellPress
OPEN ACCESS

Cell

Resource

Molecular architecture of human dermal sleeping nociceptors

Jannis Körner,[1,2,3,4,21] Derek Howard,[5,21] Hans Jürgen Solinski,[6,22] Marisol Mancilla Moreno,[7,22] Natja Haag,[4,8] Andrea Fiebig,[4,9] Anna Maxion,[4,9] Shamsuddin A. Bhuiyan,[10] Idil Toklucu,[1] Raya A. Bott,[1] Ishwarya Sankaranarayanan,[7] Diana Tavares-Ferreira,[7] Stephanie Shiers,[7] Nikhil N. Inturi,[7] Esther Eberhardt,[1,2,4] Lisa Ernst,[11] Lorenzo Bonaguro,[12,13] Jonas Schulte-Schrepping,[12,13] Marc D. Beyer,[12,13,14] Thomas Stiehl,[4,15,16,17] William Renthal,[10] Ingo Kurth,[4,8] Jenny Tigerholm,[4,15] Jordi Serra,[18] Theodore J. Price,[7] Martin Schmelz,[6] Barbara Namer,[1,4,9,19,23] Shreejoy Tripathy,[5,20,23,*] and Angelika Lampert[1,4,23,24,*]

[1]Institute of Neurophysiology, Uniklinik RWTH Aachen University, Aachen, Germany
[2]Department of Anesthesiology, Uniklinik RWTH Aachen University, Aachen, Germany
[3]Department of Intensive and Intermediate Care, Uniklinik RWTH Aachen University, Aachen, Germany
[4]Scientific Center for Neuropathic pain Aachen SCN-AACHEN, Uniklinik RWTH Aachen University, Aachen, Germany
[5]Krembil Centre for Neuroinformatics, Centre for Addiction and Mental Health, Toronto, ON, Canada
[6]Department of Experimental Pain Research, MCTN, Medical Faculty Mannheim, Heidelberg University, Ludolf-Krehl-Strasse 13-17, 68167 Mannheim, Germany
[7]The Department of Neuroscience, The University of Texas at Dallas, 800 West Campbell Rd, Richardson, TX 75080, USA
[8]Center for Human Genetics and Genomic Medicine, Uniklinik RWTH Aachen University, Aachen, Germany
[9]Research Group Neuroscience, Interdisciplinary Center for Clinical Research within the Faculty of Medicine at the RWTH Aachen University, Aachen, Germany
[10]Department of Neurology, Brigham and Women's Hospital, Harvard Medical School, Boston, MA 02115, USA
[11]Institute for Laboratory Animal Science and Experimental Surgery, Uniklinik RWTH Aachen University, Aachen, Germany
[12]PRECISE Platform for Single Cell Genomics and Epigenomics at DZNE & University of Bonn and West German Genome Center, Bonn, Germany
[13]Systems Medicine, Deutsches Zentrum für Neurodegenerative Erkrankungen (DZNE), Bonn, Germany
[14]Immunogenomics & Neurodegeneration, Deutsches Zentrum für Neurodegenerative Erkrankungen (DZNE), Bonn, Germany
[15]Joint Research Center for Computational Biomedicine (JRCC), Pauwelsstrasse 30, 52074 Aachen, Germany
[16]Institute for Computational Biomedicine and Disease Modelling with Focus on Phase Transitions between Phenotypes, Pauwelsstrasse 30, 52074 Aachen, Germany
[17]Center for Computational Life Sciences (CCLS), RWTH Aachen University, Aachen, Germany
[18]Department of Clinical Neurophysiology, King's College Hospital, London SE5 9RS, UK
[19]Department of Anaesthesiology, Intensive Care, Emergency and Pain Medicine, Zentrum Operative Medizin (ZOM), Oberdürrbacher Str. 6, 97080 Würzburg, Germany
[20]Department of Psychiatry, University of Toronto, Toronto, ON, Canada
[21]These authors contributed equally
[22]These authors contributed equally
[23]These authors contributed equally
[24]Lead contact
*Correspondence: shreejoy.tripathy@camh.ca (S.T.), alampert@ukaachen.de (A.L.)
https://doi.org/10.1016/j.cell.2025.12.048

SUMMARY

Human dermal sleeping nociceptors display ongoing activity in neuropathic pain, affecting 10% of the population. Despite advances in rodents, a molecular marker for these mechano-insensitive C-fibers (CMis) in human skin remains elusive, preventing targeted therapy. Using a Patch-seq approach, we combined single-cell transcriptomics, following electrophysiological characterization, with single-nucleus and spatial transcriptomics from pigs and integrated our findings with cross-species and human transcriptomic data. We functionally identified CMis in pig sensory neurons with patch clamp, using adapted protocols from human microneurography. We identified oncostatin M receptor (*OSMR*) and somatostatin (*SST*) as marker genes for CMis. Following dermal injection in healthy human volunteers, oncostatin M, the ligand of OSMR, exclusively modulates CMis. Our findings characterize the molecular architecture of human dermal sleeping nociceptors, providing a framework for mechanistic insight into neuropathic pain and potential therapeutic strategies.

 © 2025 The Authors. Published by Elsevier Inc.
This is an open access article under the CC BY license (http://creativecommons.org/licenses/by/4.0/).

INTRODUCTION

Neuropathic pain, which affects 10% of the population and 20%–30% of diabetic patients, correlates with increased activity of sensory neurons in the skin called by the fairly misleading name "sleeping" or "silent" nociceptors.[1–5] They are defined in human microneurography and psychophysical experiments of the skin as mechano-insensitive C-fibers (CMi-fibers,[6] also termed type 1b fibers,[7] CMis) and show pronounced chemical responsiveness, e.g., to capsaicin, ATP, partly to histamine, and to several inflammatory mediators.[8–11] Under inflammatory and other painful conditions, CMi-fibers can be sensitized to mechanical stimuli, becoming similar to polymodal nociceptors (CM-fibers or type 1a fibers[12]).

Human skin contains CMis that can be reliably identified by their distinct functional and biophysical properties.[13–16] In contrast, mice lack these homologous neurons in their skin; instead, similar neurons primarily innervate internal organs.[17] The few CMis identified in rodent skin display significantly different biophysical properties, compared with human CMis.[18–20] While mouse models crucially advance our understanding, they limit our ability to deduce molecular markers or new drug targets relevant for human skin sleeping nociceptors.[21] In contrast, pig skin is innervated by neurons resembling human CMis showing tight correlations among mechanical, chemical, and biophysical properties.[22,23] This similarity provides a valuable translational model for studying dermal nociceptive fibers relevant for human neuropathic pain. In mice, mechano-sensitivity appears less tightly correlated to biophysical properties than in humans and pigs, and the functional roles of chemosensing and disease-related hyperactivity may be assumed by other nociceptor classes.[24]

CMi-fibers are chemosensitive but insensitive to strong mechanical stimulation unless sensitized and are unable to follow high-frequency electrical pulses, even when sensitized.[16] These fibers preferentially respond to slow depolarization, such as low-frequency sinusoidal pulses rather than square pulses.[13] A characteristic feature of these fibers is their enhanced activity-dependent slowing (ADS) upon repetitive stimulation, particularly at low frequencies; when stimulated electrically in the receptive field for an extended time, the conduction velocity of action potentials (APs) traveling along the nerve fiber is reduced.[23] The distinct electrophysiological characteristics of CMis likely stem from their unique molecular architecture,[25] potentially offering an opportunity to identify specific, conserved markers for CMis. In this study, we characterize the molecular architecture of these nociceptors in pigs and humans, identifying oncostatin M (OSM) receptor (*OSMR*) and somatostatin (*SST*) as marker genes for CMis.

RESULTS

An integrated multi-modal taxonomy for pig peripheral sensory neurons

Single-cell transcriptomic studies of peripheral sensory neurons have revealed a molecular taxonomy of highly specialized and diverse cells responsible for various aspects of sensory perception like pain.[26–31] In contrast, patch-clamp studies investigating their electrical function have not yielded a similarly comprehensive cellular taxonomy based on sensory neuron excitability, especially of large mammals given their described difference in electrophysiology, compared with rodents.[32] Recent Patch-seq techniques, however, provide a unique opportunity for bridging the molecular identities of dorsal root ganglion (DRG) neurons with their electrophysiological and morphological identity[33–37]—individual neurons are electrically characterized via patch clamp, followed by single-cell RNA sequencing (scRNA-seq).

We used Patch-seq to characterize electrophysiological and transcriptomic characteristics of pig DRG neurons, intentionally targeting smaller, likely C-fiber neurons. We assessed up to 27 electrophysiological features per cell and visualized cellular morphologies prior to capturing whole-cell mRNA (Figure S1). We successfully sampled 267 neurons using our improved harvesting protocol (Data S1; STAR Methods) and analyzed their transcriptome by Smart-seq2 and deep sequencing. Of these, 226 neurons passed rigorous quality control of transcriptomes, with a median of 700,000 reads and 11,000 unique detected genes per cell (Data S1), demonstrating the deep transcriptomic characterization provided by this methodology.

We next applied droplet-based single-nucleus RNA sequencing (snRNA-seq), using the 10× Genomics Chromium v3 platform to sample transcriptomes from 16,997 nuclei from flash-frozen pig DRG. Following rigorous quality control, we obtained 2,176 DRG neuronal nuclei, with a median of 4,574 detected unique molecular identifiers (UMIs) and 2,131 genes expressed per nucleus. Following unsupervised clustering of snRNA-seq-based transcriptomes, we identified 16 DRG neuronal subtypes based on distinct marker gene expression (Figure 1A; see STAR Methods). Important pain-related genes, such as the calcitonin-related polypeptide beta (*CALCB*) or the receptor for OSM (*OSMR*), were reliably quantified, while a few, including *SCN10A* and *TRPV1*, suffered from some degree of genome annotation incompleteness in the pig, as described previously (Data S1).[38] Despite this, the transient receptor potential channel *TRPV1* expression was detected in expected neuronal subtypes (Data S1), ensuring that these genome annotation limitations did not impede our ability to identify its presence where anticipated.

We mapped each Patch-seq characterized cell to our larger snRNA-seq atlas by gene expression guided integration of the two datasets (Figure 1A; see STAR Methods). Each transcriptomically defined sensory neuron subtype was represented by at least 1 and up to 74 Patch-seq characterized neurons (Figure 1B); we reason that the difference in cell numbers per transcriptomic type is likely related to our sampling strategy targeting smaller cells for characterization. The integration of snRNA-seq and Patch-seq datasets effectively mitigated technical differences between the two approaches, as evidenced by the uniform distribution of cells from different batches and biological replicates across the integrated uniform manifold approximation and projection (UMAP) space (Data S1). While we observed some expected differences in injury-induced and culturing-related genes between the datasets[39,40] (Data S1), cell-type-enriched marker genes were largely consistent between either technology (Data S1). Patch-seq cells, which are mapped to the same molecular cell type, display similar

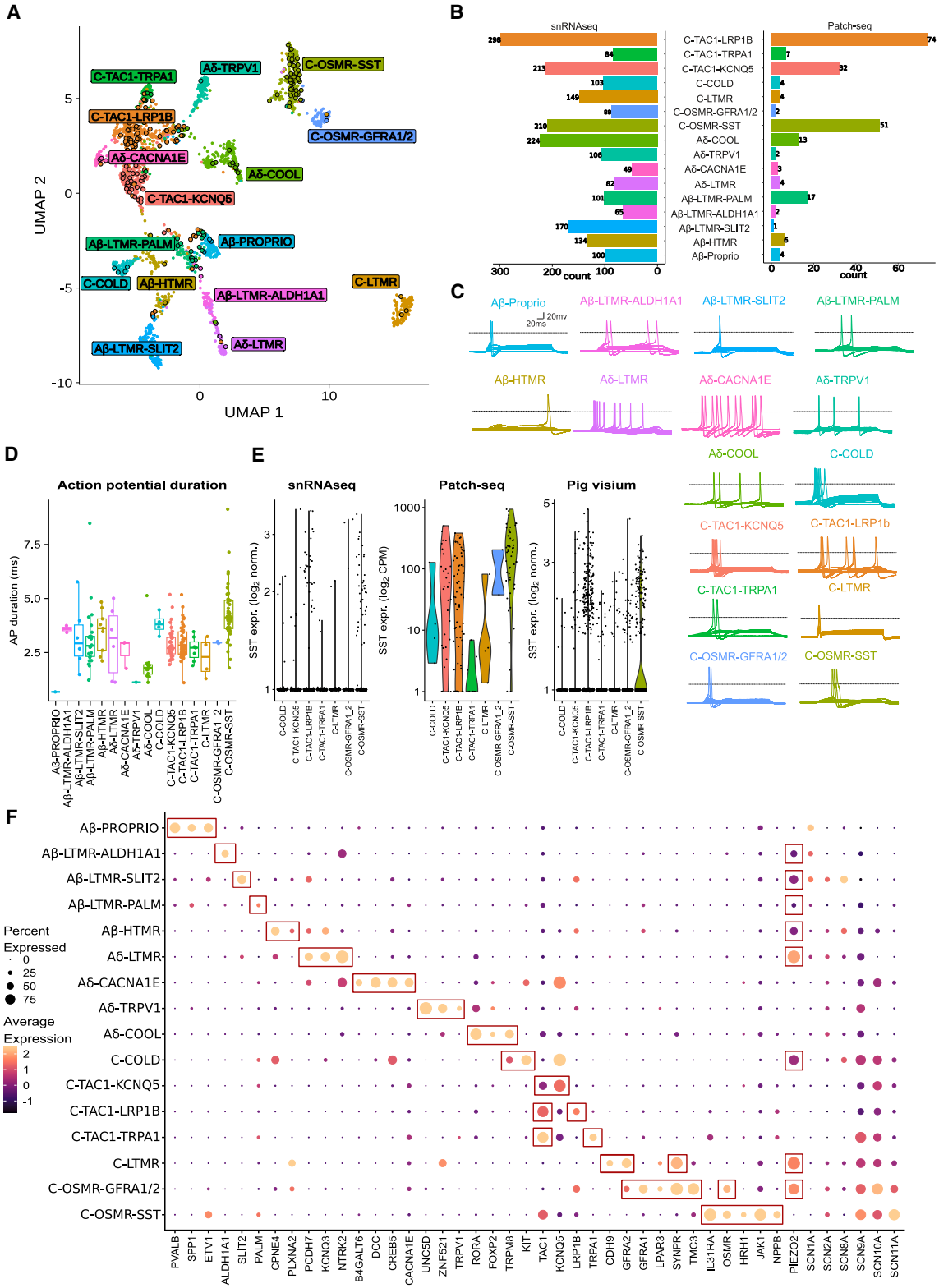

Figure 1. A multi-modal taxonomy of pig DRG neurons

(A) Multi-modal neuronal taxonomy of porcine DRG, displaying DRG neuronal subtypes categorized by multivariate gene expression profiles from snRNA-seq (small dots) and Patch-seq (larger circles). Colors indicate neuronal identity based on unbiased clustering of snRNA-seq data.

(legend continued on next page)

electrophysiological properties (Figure S1); however, we note that clustering cells based on basic electrophysiological parameters alone (e.g., resting membrane potential and AP threshold) was generally insufficient to capture the known diversity of DRG neuronal cell types, with the exception of the Aδ-COOL group (Data S1).

To corroborate our findings, we also performed "spot-based" spatial transcriptomics (Visium technique) from pig DRG neurons (Figure S2), using the same approach as reported before for human DRG neurons,[29] with identification of 5,577 putative neurons with a median of 4,597 detected UMIs and 2,138 expressed genes per spot (Data S1). Our thorough taxonomy reflects all major expected neuronal DRG populations, consisting of five Aβ-, four Aδ-, and seven C-fiber-related neuronal subtypes (Figure 1; Table S1). In naming the cell types in this study, we designated putative fiber types based on gene expression patterns and knowledge of fiber function in large mammals and through comparisons with existing transcriptomic datasets from large mammals, such as humans and monkeys.[27,29,31] With our approach, we were able to map distinct electrophysiological and morphological features to the transcriptomic identities of the sensory neurons (Figures 1C, S1, and S2), e.g., the groups related to C-fibers, compared with A-fibers, exhibited significantly longer AP durations (Figure 1D) and, as expected, had smaller mean diameter cell bodies (Figure S2).

The Aβ-group of putative proprioceptors, Aβ-Proprio, displayed high expression of *PVALB*, *SPP1*, and *ETV1*, hyperpolarized afterhyperpolarization (AHP) minimum (−81.6 ± 1.22 mV) and hyperpolarized AP thresholds (−55.2 ± 4.31 mV), and large cell diameters (95 ± 3.1 μm) (Figures 1F, S1, and S2). We identified three low-threshold mechanoreceptor subtypes (Aβ-LTMRs), termed Aβ-LTMR-ALDH1A1, Aβ-LTMR-SLIT2, and Aβ-LTMR-PALM, each expressing *PIEZO2* and showing low expression of the pain-related sodium channel genes *SCN9A*, *SCN10A*, and *SCN11A*. The Aβ-fiber neuron group named Aβ-HTMR likely represents high-threshold mechanoreceptors, marked by *CPNE4* and *PLXNA2*, as well as *PIEZO2* and *SCN10A*, suggestive of a potential nociceptive function.[29]

We identified four Aδ groups: Aδ-LTMR, with uniquely high expression of *PIEZO2* and marked by *PCDH7*, *KCNQ3*, and *NTRK2*; Aδ-CACNA1E, marked by *B4GALT6*, *DCC*, *CREB5*, *CACNA1E*, and— unique among Aδ-fibers— by its relatively high expression of *SCN10A*; Aδ-TRPV1, marked by *UNC5D* and *ZNF521* and with distinctively high expression of the capsaicin and heat receptor *TRPV1*; and Aδ-COOL, marked by the cold- and menthol-sensitive ion channel *TRPM8*, *RORA*, and *FOXP2* expression. Aδ-COOL displayed a very short AP duration (2.01 ± 0.286 ms; Figure 1D), low AP amplitudes (97.5 ± 2.31 mV), and the highest fraction among all DRG cell types for ongoing activity (61.5%; Figure S1), potentially due to patch clamp being performed at room temperature that represents a tonic cold stimulus for those cells.

The C-fiber-related groups all displayed high expression of the pain-related sodium channel genes *SCN9A*, *SCN10A*, and *SCN11A*. C-COLD was marked by *TRPM8* and *KIT* and showed moderate *PIEZO2* expression, suggesting potential mechanosensitivity. We identified three C-fiber-related subtypes with high expression of *TAC1*, encoding for the nociception-related neurotransmitter substance P, and each subtype showed APs with large amplitudes (Figure S1). These three populations differed by strong expression of the potassium channel *KCNQ5* (C-TAC1-KCNQ5), the low-density lipoprotein receptor-related protein 1B (*LRP1B*; C-TAC1-LRP1B), and the pain-relevant transient receptor potential channel *TRPA1* (C-TAC1-TRPA1).

One C-fiber subtype was marked by *CDH9* and displayed high expression of *PIEZO2* and *GFRA2*; we termed these cells C-LTMRs, given the expression of similar markers in a putative orthologous DRG cell type described in humans and mice previously.[29,30] We identified an additional group of C-fibers, termed C-OSMR-GFRA1/2, expressing the OSMR and marked by the expression of *GFRA1*, *GFRA2*, *SYNPR*, and *TMC3*, as well as high *PIEZO2* expression, suggestive of potential mechanosensitivity. Finally, we identified a distinct C-fiber subgroup, notable for its high expression of *OSMR* (Data S1) and low expression of *PIEZO2* and marked by *IL31RA*, the histamine receptor HRH1, *JAK1*, and *NPPB*. We named this subgroup C-OSMR-SST, because while *SST* mRNA was not reliably detected among our single-nucleus data, we observed prominent expression of *SST* in these cells in our whole-cell datasets of these neurons (i.e., Patch-seq and spatial transcriptomics; Figure 1E; Data S1). Notably, these cells expressed the highest levels of *SCN11A* and displayed the longest AP duration of any DRG cell type in our dataset (Figure 1D).

In summary, our pig DRG neuronal taxonomy displays marked neuronal diversity in transcriptomic and electrophysiological characteristics.

Comparison of pig DRG transcriptomes to cross-species atlases, including human

Transcriptomic studies of sensory neurons have shown evolutionary conservation of major cell identities between species.[26,41] Consequently, to contextualize our pig DRG cell-type taxonomy in

(B) Overall counts of cells in each neuronal subtype from snRNA-seq (left) and Patch-seq (right).
(C) Representative current-clamp voltage traces for exemplary cells characterized via Patch-seq for each cell type in (A). Overlay of responses to 200 ms rectangular depolarizing current pulses of increasing intensities. Scale bar insets represent 20 ms (horizontal) and 20 mV (vertical). Dashed line indicates 0 mV.
(D) Distributions of AP duration (C-fibers: 3.34 ± 0.082 ms, A-fibers: 2.75 ± 0.196 ms, $p = 8.88 \times 10^{-5}$, two-sided Wilcoxon rank-sum test). Longest AP duration for C-OSMR-SST: 4.26 ± 0.170 ms, $p = 6.69 \times 10^{-11}$, two-sided Kruskal-Wallis test for each neuronal subtype (mean ± SEM).
(E) *SST* expression in snRNA-seq (left) and Patch-seq (middle) and spatial transcriptomics (right). Each point represents a single cell, with expression quantified by RNA-seq read counts and displayed on a log-transformed *y* axis. Difference in units between axes related to technological differences.
(F) Group dot plot illustrating snRNA-seq-based expression of specific genes for each neuronal subtype. Inset boxes reflect representative markers or cell-type-relevant genes discussed in the text.
See also Figures S1 and S2, Table S1, and Data S1, S2, and S3.

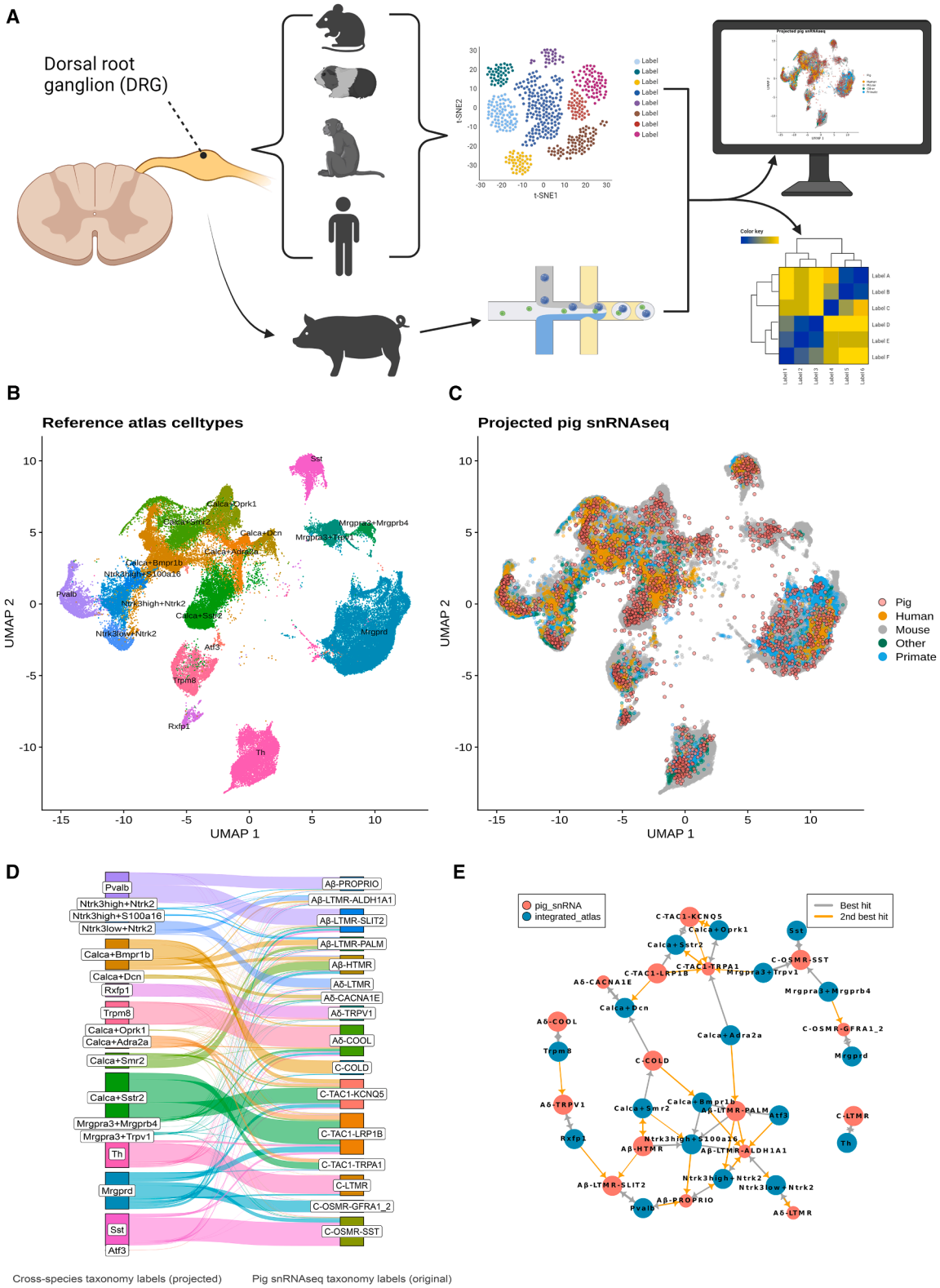

Figure 2. High concordance between pig and cross-species neuronal taxonomies

(A) Schematic overview of the workflow to compare pig and cross-species neuronal taxonomies.

(B) UMAP visualization of cell types in the cross-species DRG atlas, with each cluster (colors) representing a distinct DRG neuron cell type.

(legend continued on next page)

relation to homologous cell types defined in other species, including humans, we compared the transcriptional identities from our pig snRNA-seq dataset with a recently published cross-species atlas of the mammalian DRG (Figure 2A).[41] Following the projection of our pig snRNA-seq dataset onto this atlas (see STAR Methods), we observed a good representation of pig neuronal nuclei among the cell-type clusters defined in this broader cross-species atlas (Figures 2B and 2C).

To quantify the comparability between the pig and cross-species DRG taxonomies, we employed two complementary analytical approaches. First, we used a Seurat-based label transfer method to project the cross-species atlas cell-type labels onto our pig snRNA-seq data. This approach predicts cell-type labels for query cells based on transcriptional similarities to the reference dataset. We visualized these results using a river plot (Figure 2D), which illustrates the flow of cell-type assignments from the cross-species classification to our original pig taxonomy. Second, we applied the MetaNeighbor algorithm[42] to evaluate the replicability of cell types across taxonomies. This method quantifies the similarity of entire cell-type groups based on shared gene expression patterns. We represented these MetaNeighbor scores using a clustergraph plot (Figure 2E), where edge weights indicate the strength of cell-type similarity across taxonomies. For each pig cell type, the top corresponding cell type in the cross-species atlas and its MetaNeighbor area under the curve (AUC) score are provided in Table S1.

Overall, we observed largely concordant cell-type nomenclatures, with several examples of strong one-to-one orthologous relationships (delineated in Table S1), such as between SST (cross-species) and C-OSMR-SST (pig), Mrgprd (cross-species) and C-OSMR-GFRA1/2 (pig), Th (cross-species) and C-LTMR (pig), and Trmp8 (cross-species) and Aδ-COOL (pig), among others. Additionally, we identified a few one-to-many relationships; for instance, the cell type classified as Pvalb within the cross-species atlas corresponded to two cell types in our pig taxonomy, Aβ-PROPRIO and Aβ-LTMR-SLIT2. We also noted that certain cell types, such as Mrgpra3 + Mrgprb4 and Mrgpra3 + Trpv1, defined in the cross-species atlas largely based on their prevalence in rodents were less frequent in our pig dataset, suggesting that they may be underrepresented in larger mammals like pigs and humans.

Additionally, we performed a similar analysis for a recently published mouse genetic toolkit, in which the transcriptomic identity of rodent sensory neurons was linked to cell morphology, cutaneous innervation areas, as well as mechanical and thermal thresholds[20] (Figure S3). We observed excellent concordance between cell types and several one-to-one orthologous relationships (see Table S1). Also, here, we identified a few one-to-many relationships; for instance, the cell type classified as *CGRP-γ* within the rodent atlas corresponded to two cell types in our pig taxonomy, C-TAC1-TRPA1 and Aβ-LTMR-SLIT2.

While cross-species comparisons offer broad evolutionary insights, they may not fully capture the nuances of larger mammalian systems, particularly for pain-relevant neuronal populations. For instance, the neurons called CMi that are characterized by a lack of mechano-sensitivity, the presence of chemosensitivity, and specific biophysical properties in human and pig do not seem to have a corresponding fiber type innervating the mouse skin but are crucial in human nociception. Also, *TRPM8*-positive neuron organization differs between rodents and primates.[31]

Given this translational gap to human physiology, we conducted a similar comparative analysis using recent transcriptomic datasets composed exclusively of human DRG cells,[26,29,31] offering a more focused evaluation of the alignment of our pig cell types with those in humans (Figure S3). Here, we also observed a strong correspondence between the cell types defined in our pig DRG taxonomy and those identified in human-specific atlases. These analyses also showed that some marker gene products previously used for the definition of neuronal subgroups, like *CHRNA3*, are not expressed in orthologous cell types between mice and human (Figure S3).

These analyses further reinforce the notion that the pig serves as a robust model for studying human sensory neurobiology, with pig DRG cell types closely aligning with those found in humans, both within the broader cross-species context and within the more specific framework of human-focused taxonomies.

Identification of C-OSMR-SSTs as probable sleeping nociceptors

Having described the pig DRG neuronal taxonomy and having confirmed its validity to human DRG, we aimed to identify the subgroup that represents the sleeping nociceptors within those DRG neuronal subtypes. CMi-fibers can be reliably identified in humans and pigs *in vivo* by a combination of three functional electrophysiological characteristics. To transfer this *in vivo* stimulation paradigm to our *in vitro* experiments, we applied our optimized Patch-seq electrophysiological characterization pipeline (Figure 3).

First, we applied a train of 75 suprathreshold stimulations delivered at 2 Hz to the patched cells to assess ADS (n = 176 cells).[43] High amount of activity, e.g., due to a 2-Hz stimulation in sleeping nociceptors in human or pig skin *in vivo*, induces substantial slowing of conduction velocity (Figures 3A–3C[23]). C-OSMR-SST neurons displayed more ADS, compared with other C-fiber-related classes (Figures 3D and S4). During the stimulation, the C-OSMR-SST neurons displayed significant activity-dependent membrane potential hyperpolarization, reduced AP peak, and

(C) Projection of pig snRNA-seq cells (red dots) onto the cross-species atlas (same as B, cells colored by species of dataset origin).
(D) River plot illustrating the cell-type correspondence of pig snRNA-seq cells after projecting into cross-species taxonomy (left) and original pig snRNA-seq taxonomy labels (right, cell-type colors same as in Figure 1). Width of connecting line strips indicates the count of pig snRNA-seq cell mapping between categories.
(E) MetaNeighbor cluster graph visualization showing the relationship between pig snRNA-seq cell types (red nodes) and cross-species taxonomy cell types (blue nodes). Edges represent strong similarities between cell types, with thicker edges indicating stronger associations. Best hits (gray lines) indicate closest cell types by co-expression, whereas 2nd best hit (orange lines) indicates second closest cell type.
See also Figure S3.

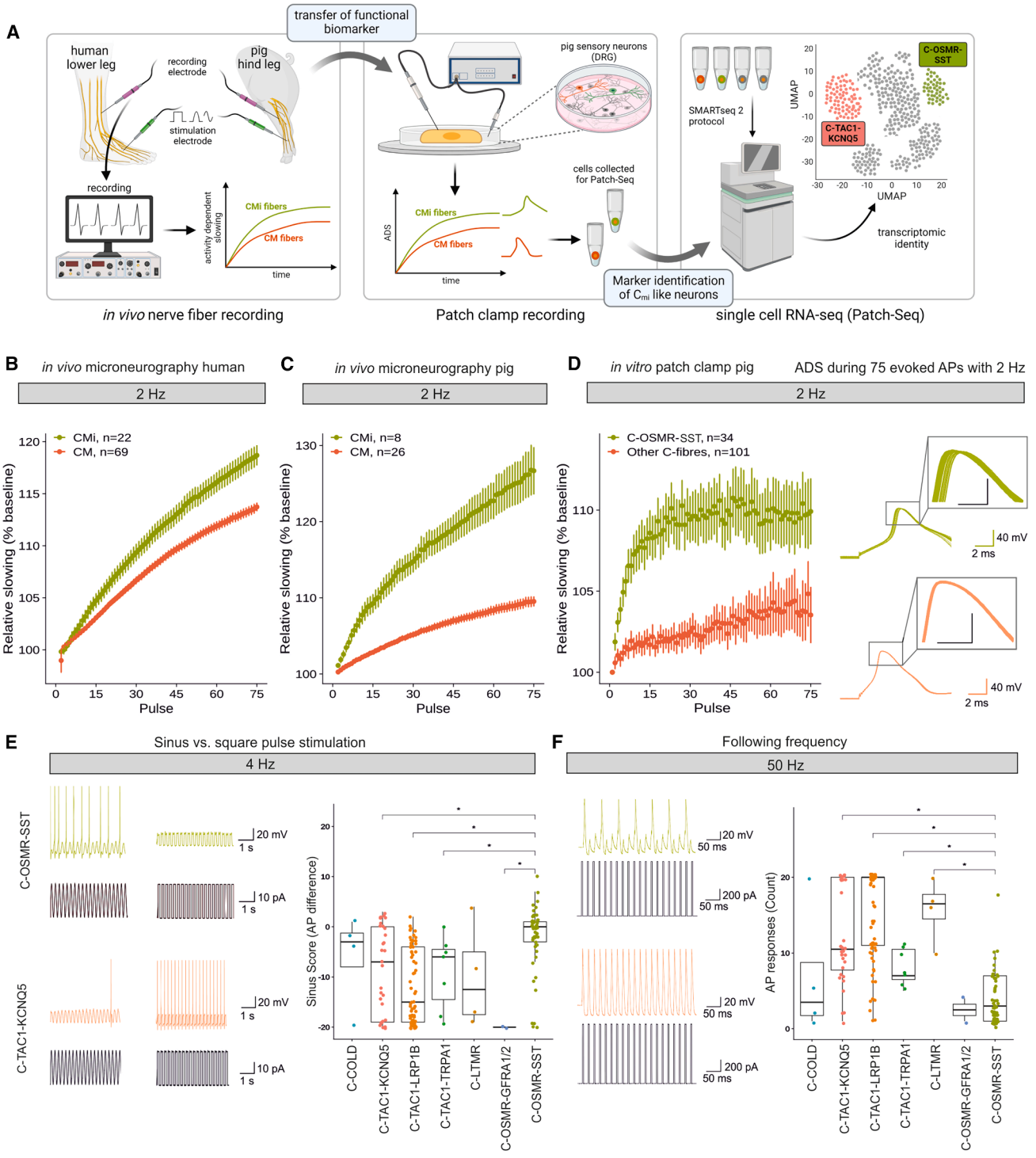

Figure 3. Molecular identity of CMis in Patch-seq and adapted electrophysiological stimulation protocols *in vitro*

(A) Schematic for identifying molecular markers of CMis. CMis are traditionally identified *in vivo* using electrical stimulation protocols applied to the skin (left). Functional biomarkers of CMis include ADS upon repetitive stimulation, observed in CMis but not mechano-sensitive C-fibers (CMs). We transferred these CMi-discriminating functional biomarkers into electrophysiological stimulation protocols that can be applied to DRG neurons, using patch clamp recordings *in vitro* (middle). This enables identifying molecular markers of putative CMi-like neurons, using transcriptomics from Patch-seq (right). Data are presented as mean ± SEM.

(B and C) *In vivo* characterization of ADS (*y* axis) relative to stimulation pulse number (*x* axis) for CMi-fibers (green) and polymodal CMs (red) in humans (B) and pigs (C).

(legend continued on next page)

AP maximum upstroke slope relative to other C-fiber cells (Figures S4A–S4C).

Second, trains of 20 sine wave and square pulses were delivered at 4 Hz (i.e., sinus score, see STAR Methods, n = 213 cells) to assess the preference for sine waves vs. square pulses observed *in vivo* for sleeping nociceptors.[13,16,23] The C-OSMR-SST subgroup demonstrated the highest sinus score (Figure 3E, right).

Third, trains of 20 short suprathreshold square pulses were delivered at 50 Hz (n = 226 cells; Figure 3F), as CMi-fibers *in vivo* are unable to respond to high-frequency stimulation continuously with AP generation (i.e., they have a lower following frequency[13,16,23]). The C-OSMR-SST subtype displayed the fewest AP responses, significantly lower compared with the C-TAC1-KCNQ5, C-TAC1-LRP1B, C-TAC-TRPA1, and C-LTMR subtypes (Figure 3F, right), with the exception of the C-OSMR-GFRA1/2 cells of which only two were recorded.

To further validate our inference that C-OSMR-SST neurons likely correspond to sleeping nociceptors (CMis), we conducted an independent analysis to determine whether neurons with CMi-like electrophysiological features also express genes overlapping with C-OSMR-SST markers. First, we performed a principal-component analysis (PCA) on all included neurons regardless of transcriptomic identity, incorporating the three functional hallmarks of CMis—ADS, sine wave affinity, and reduced following frequency at 50 Hz—along with AP duration (Figure 4A). As expected, the first principal component (CMi ephys PC1) accounted for the majority of variance in these features (49%), indicating that this component could serve as a single score for CMi-like neuronal identity. Leveraging gene expression profiles collected from the same neurons via Patch-seq, we performed a transcriptome-wide analysis to identify genes significantly associated with "CMi scores" (Figure 4B). We found a substantial overlap between these electrophysiology-based CMi-associated genes and markers of C-OSMR-SST neurons (Figures 4C, 76 genes out of 228 total CMi-associated genes, p value for hypergeometric test = 2.34×10^{-79}). This analysis further highlighted several key pain-related ion channels, including but not limited to SCN11A (Figures 4D and S5) and *SCN10A* (for which recently a new blocker was approved as pain medication in clinics),[44] suggesting that their expression is closely related to CMi-like neuronal characteristics and underscoring the therapeutic value of targeting these channels (see discussion). Previous data suggest a fundamental role of SCN11A in human pain perception[45] and pain syndromes.[46]

To establish a mechanistic link between the gene expression pattern of genes coding voltage-gated sodium channels and the functional phenotype of C-OSMR-SST neurons, we used the expression data of these neurons from the snRNA-seq dataset to generate a computational model based on an extension of the Hodgkin-Huxley approach by using the modeling framework from Köster et al.[47] (see STAR Methods). In this model, for instance, reduction of the SCN11A conductance of 50% leads to a strong reduction of the AP duration from 1.36 to 1.18 ms (Figures 4E and S6). The long AP duration as well as the AP slope of C-OSMR-SST neurons were highly dependent on the expression of SCN11A, suggesting that this channel is a key player in shaping the characteristic functional phenotype of CMi-fibers.

Altogether, our *in vitro* experiments, modeled on adapted *in vivo* microneurography stimulation protocols, demonstrate that C-OSMR-SST neurons exhibit functional properties similar to those of CMi-fibers identified in human skin *in vivo*.

OSM selectively modifies CMi-fibers *in vivo* in humans

Our experiments suggest that C-OSMR-SST neurons are strong candidates for molecularly defined CMi-fibers in pigs and humans. To determine whether OSMR expression identifies functional sleeping nociceptors in humans, we applied OSM, the ligand for OSMR, intradermally to healthy volunteers and assessed potential variation of typical CMi-fiber reactions, such as axon reflex erythema (flare) and ADS. Co-application with histamine was used to study potential sensitizing effects of OSM on histamine-mediated CMi-fiber activation. (Figure 5A).

Intradermal injection of OSM (500 ng in 20 μL) into the forearm skin of healthy volunteers induced a biphasic flare response. During the acute phase (0–15 min), co-injection of OSM with histamine (0.01%) produced a significantly increased axon reflex flare, compared with histamine alone, in line with enhanced CMi-fiber activation (Figures 5B, 5C, and S7; Table S2).[48,49] During the subacute phase (1–24 h), OSM alone led to a delayed but clearly detectable flare in 7 out of 7 participants. This effect was not observed following vehicle injection or histamine alone, indicating that OSM can trigger a flare response by itself.

To provide additional evidence of preferential CMi-fiber manipulation by OSM, we performed single nerve fiber recordings (microneurography) from the superficial fibular nerve in 7 healthy human volunteers, analyzing a total of 60 identified C-fibers (25 CMi-fibers and 35 CM-fibers) (Figure S7). CMi-fibers exhibited a clear, typical ADS at 0.25 Hz stimulation. Following vehicle injection, ADS in CMi-fibers declined time dependently,

(D) Similar to (B) and (C), showing ADS from Patch-seq-characterized neurons stimulated using somatic current injection. Cells colored by molecular cell type, highlighting differences between C-OSMR-SST cells (green, 110% ± 2.04%, n = 34), compared with all other C-fiber neurons in Patch-seq dataset (red, 104% ± 1.73%, n = 110, $p = 9.27 \times 10^{-7}$, Mann-Whitney U = 741.5). Right panel shows overlay of 75 APs induced by 1 nA current injection for 10 ms delivered at 2 Hz from an example C-OSMR-SST (top) and C-TAC1-KCNQ5 neuron (bottom). Note that APs become more delayed over the course of the stimulation protocol, especially in the C-OSMR-SST neurons but comparatively less so in the C-TAC1-KCNQ5 neurons.

(E) Left, representative voltage trace (top) and current stimulation (bottom) traces evoked by sinusoidal (left) vs. square pulse stimulation (right). Right, quantification of neuronal sinus scores across C-fiber neurons characterized via Patch-seq. Sinus scores are defined as the difference in AP count evoked between sinusoidal vs. square pulse stimuli; positive scores indicate greater CMi-like activity. ANOVA ($F(6, 158) = 9.03$, $p < 0.00001$).

(F) Left, illustration of calculation of following frequency, where neurons are stimulated with 20 1 nA current pulses for 4 ms at 50 Hz. Right, count of AP responses evoked by 50 Hz stimuli designed to assess efficacy to follow high-frequency stimuli; fewer evoked APs indicate greater CMi-like activity. Asterisks denote statistical significance with $p < 0.05$ as determined by an ANOVA ($F(6, 166) = 24.59$, $p < 0.0001$) followed by Tukey's post hoc honest significant difference (HSD) test.

See also Figure S4.

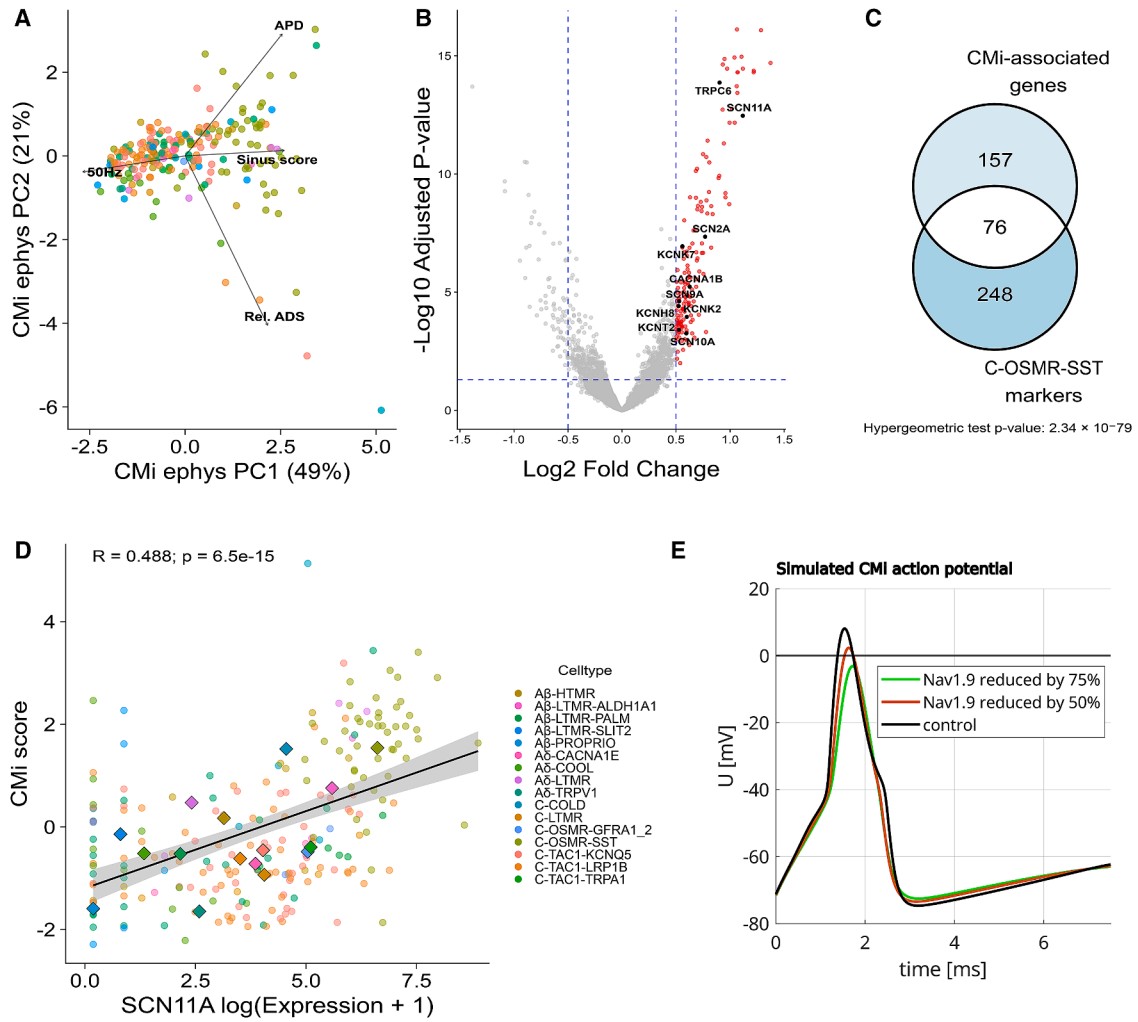

Figure 4. Electrophysiological feature guided analysis of genes associated with CMi phenotype

(A) PCA biplot of CMi-related electrophysiology features. Each point represents a single neuron, colored by cell type. Arrows indicate the contribution of each electrophysiological feature to the principal components.

(B) Volcano plot showing CMi score-associated genes. Axes indicate magnitude (*x* axis) and statistical significance (*y* axis) of association between gene expression and CMi score. Red dots indicate significantly differentially expressed genes (adjusted $p < 0.05$ and $\log_2$ fold change > 0.5). Black dots highlight ion channel genes. Vertical blue dashed lines indicate $\log_2$ fold change thresholds, and the horizontal blue dashed line indicates the adjusted *p* value threshold.

(C) Venn diagram illustrating the overlap between CMi-associated genes (red genes highlighted in B) and C-OSMR-SST markers (derived from snRNA-seq data).

(D) Correlation between SCN11A expression and CMi score. Each point represents a single neuron, colored by cell type. Larger diamond-shaped points indicate the mean expression and CMi score for each cell type. The black line shows linear regression fit with 95% confidence interval.

(E) Simulated AP shapes demonstrating the effect of reducing Nav1.9 (*SCN11A*) conductance. Black trace shows control condition, while red and green traces show the effects of 50% and 75% reductions in Nav1.9 conductance, respectively, illustrating the channel's contribution to AP characteristics.

See also Figures S5 and S6 and Methods S1.

consistent with prior findings.[50] This drop was markedly reduced in CMi-fibers receiving OSM injection in their receptive field (Figures 5D, 5E, and S7; Table S3), indicating that OSM selectively modifies CMi-fiber conduction properties. In contrast, in CM-fibers—mechano-sensitive, polymodal nociceptors that do not exhibit significant ADS at 0.25 Hz—an OSM-mediated manipulation was absent, confirming the specificity of the effect.

Most CMi-fibers remained mechanically unresponsive before and after injection of either vehicle or OSM during microneurography recordings, except for two CMi-fibers whose response following OSM was minor (Figure S7). CM-fibers remained stably mechano-sensitive across all time points and conditions. In a psychophysical assay, von Frey hair and brush testing at baseline, 15 and 60 min and up to 24 h following injection, revealed no consistent changes in mechanical sensitivity (Figure S8). Quantitative psychophysical testing in seven participants showed no relevant changes in itch or pain perception during or after OSM injection, compared with vehicle (Figure S8; Tables S4 and S5). Subjective ratings remained low across all time points, and co-injection of OSM with histamine did not

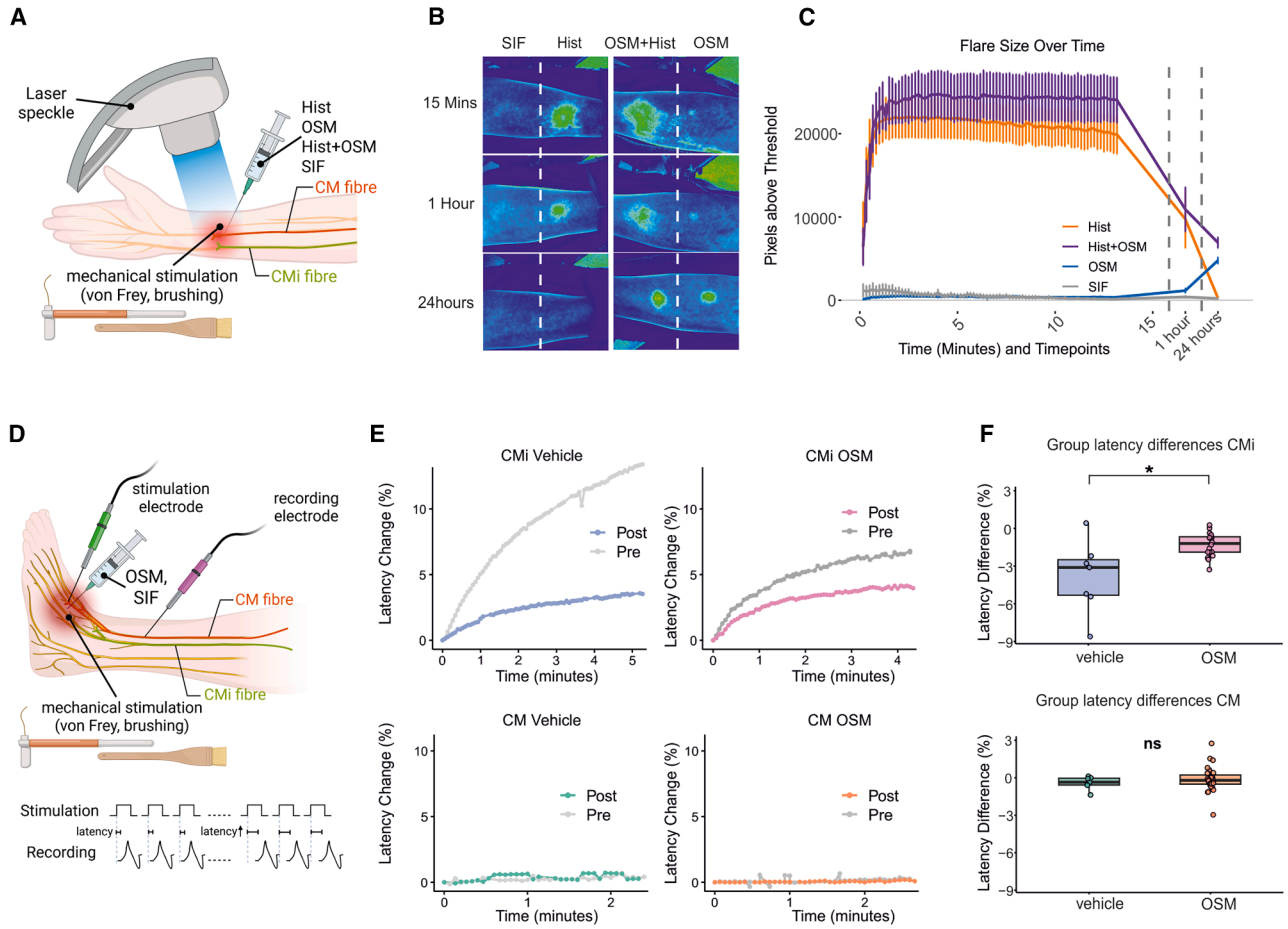

Figure 5. Applying OSM in humans *in vivo* selectively affects CMi-fibers

(A) Schematic of the experimental setup showing intradermal injection of OSM and subsequent superficial blood flow measurements in humans.

(B) Representative laser speckle contrast images from injection sites receiving synthetic interstitial fluid (SIF), histamine (Hist), OSM alone, or histamine + OSM (Hist + OSM).

(C) Quantification of flare area over time. $n = 7$ for acute and 1-h measurements; $n = 6$ for 24-h measurements.

(D) Schematic of the experimental setup showing intradermal injection of OSM and subsequent microneurography measurements in humans.

(E) Representative microneurography traces from CM- and CMi-fibers before (gray) and after (colored) injection of SIF (vehicle) alone or SIF + OSM. *y* axis indicates relative change in AP latency (i.e., ADS) in response to 0.25-Hz test pulses. Datapoints deviating >2.5% from the last sample point are filtered.

(F) Quantification of post-pre latency changes across fiber types and conditions. CM-fibers: $n = 8$ vehicle, $n = 27$ OSM; CMi-fibers: $n = 7$ vehicle, $n = 18$ OSM. Statistical analysis was performed using independent Kruskal-Wallis tests, mean ± SEM. For CM-fibers, no significant difference was observed ($Chi^2 = 0.588$, df = 1, $p = 0.4432$). In contrast, CMi-fibers showed a significant difference between OSM and vehicle groups ($Chi^2 = 5.865$, df = 1, $p = 0.0154$).

See also Figures S7 and S8 and Tables S2–S5.

increase perceptual responses relative to histamine alone (Figure S8).

These findings provide direct functional evidence that OSM selectively modulates CMi-fibers in human skin, likely by directly interacting with OSMR on these fibers. Thus, OSMR is likely to serve as a marker of this sleeping nociceptor population, consistent with the molecular identity of C-OSMR-SST neurons.

DISCUSSION

The research described here examines the molecular and functional organization of sensory neurons involved in pain processing by directly integrating physiological and transcriptomic data at the level of individual cells. The dataset systematically links the electrophysiological properties with single-cell transcriptomic profiles across sensory neuron subtypes. By combining *in vivo* and *in vitro* physiology with multiple single-cell and spatial transcriptomic approaches in pigs and humans, we characterize the expression patterns of a neuronal population consistent with functionally defined human dermal CMis, known as sleeping nociceptors. This integrative approach provides a framework for examining molecular pathways associated with spontaneous activity in neuropathic pain.[1–4]

The molecular architecture of C-OSMR-SST neurons

Our multi-modal analysis identified the C-OSMR-SST cluster as the probable CMi population. This cluster exhibits a molecular

architecture that may directly explain hallmark CMi properties, such as most notably their distinctive ADS and capacity for sensitization. This subgroup expresses the highest level of *SCN11A*, which codes for the voltage-gated sodium channel Nav1.9, a protein intensely discussed as a drug target for neuropathic pain.[51,52] We hypothesized that Nav1.9, in combination with other channels expressed in this neuron type, including *SCN10A*/Nav1.8, gives rise to the distinct functional characteristics of C-OSMR-SST neurons, including their sine wave sensitivity and the formation of very broad APs.[51,53] Mechanistically, Nav1.9's ultra-slow inactivation kinetics provide a plausible basis for ADS; during repetitive activation, the slow inactivation may more strongly depolarize the cell membrane, thus inducing progressive inactivation and slow conduction, consistent with microneurographic profiles of CMi-fibers. In our unbiased transcriptome-wide correlation analysis, *SCN11A* expression showed a strong positive relationship with a composite CMi score that integrates ADS and sine wave sensitivity, reinforcing this mechanistic link. To explore its functional relevance, we used the sodium channel expression data from this study to inform a computational model of CMi-fibers, based on Köster et al.[47] This model revealed a substantial contribution of Nav1.9 to the steepness of the AP upstroke and the shoulder. Together, these *in silico* and correlative data indicate that high Nav1.9 conductance is a defining molecular feature underlying CMi excitability and ADS. Our findings are consistent with a prominent role of Nav1.9 in CMi-fiber electrogenesis and the promise for developing modulators of Nav1.9, as these might be especially effective in silencing sleeping nociceptors. We acknowledge that expression-level correlation alone cannot establish causality and that direct genetic or pharmacological manipulation will be essential in future studies. Our multi-pronged rationale—including expression specificity, prior pain-related research, electrophysiological alignment, and modeling insights—supports Nav1.9 as a strong candidate channel contributing to CMi excitability. Importantly, the dataset enables the exploration of additional ion channels and modulators that may contribute to the function and modulation of human dermal sleeping nociceptors.

In addition to its ion channel profile, the C-OSMR-SST subgroup is defined by high expression of OSMR and its downstream signaling partner januskinase (JAK1).[54] Given that OSM impacts function of CMi-fibers, this signaling axis may represent a key sensitizing pathway. The co-expression of OSMR, JAK1, HRH1, and interleukin (IL)-31RA defines a distinctive "sensitization repertoire," priming these neurons to respond to inflammatory mediators. We speculate that under pathophysiological conditions, activation of the OSMR/JAK1 pathway could modify the CMi-fiber phenotype to support sensitization. A subset of CMi-fibers is histamine sensitive and associated with itch, and notably, JAK-inhibitors are already in clinical use as antipruritic agents.[55] Interfering with JAK signaling may therefore prevent CMi-fiber sensitization, potentially counteracting the development of neuropathic pain and chronic itch beyond its known anti-inflammatory effects.[56,57]

In vivo validation and functional nuances in humans

Our human experiments using psychophysics, flare response quantification, and microneurography provide direct functional evidence that OSM selectively modulates CMi-fibers in human skin, likely via activation of OSMRs expressed on these neurons. While OSM alone did not induce mechanical sensitization or subjective itch or pain, it significantly enhanced histamine-induced flare responses, which is a well-established surrogate for CMi-fiber activation.[22] The enhancement of histamine-induced flare responses following OSM co-injection provides compelling evidence for a direct action of OSM on OSMR-expressing CMi-fibers. This is consistent with previous *in vitro* work showing that OSM can acutely increase histamine responses and excitability in rodent and human sensory neurons.[48,58] Moreover, in rodent models, these effects are abolished in OSMR-deficient neurons, further confirming a direct neuronal mechanism.[48] Our human *in vivo* data now extend these findings by demonstrating that similar acute neuronal modulation occurs in intact peripheral nerves, supporting the translational relevance of OSMR signaling in sleeping nociceptor function. Microneurography data further indicate that OSM modifies the conduction dynamics of CMi-fibers, as reflected by reduced decline in ADS over time, compared with vehicle. While the precise functional meaning of this altered ADS remains to be determined, its fiber-specific nature further supports a selective interaction between OSM and CMi-fibers. Importantly, these effects were absent in CM-fibers, and psychophysical testing confirmed a lack of generalized sensitization. Together, these findings support OSMR as a functional and molecular marker of human CMi-fibers and point to OSMR/JAK1 signaling as a possible modulator of sleeping nociceptor activity in humans.

A conserved transcriptome with a divergent function

Our analyses demonstrate that the C-OSMR-SST cell type is highly transcriptionally conserved across mammals, yet its functional phenotype appears to have diverged significantly. This presents a key paradox; in pigs and humans, the electrophysiological and molecular profile of this cluster aligns with CMis, whereas in mice, the transcriptomically orthologous Sst-positive neurons have been identified as mechano-sensitive C-HTMRs.[20] This functional divergence extends to their skin innervation and anatomy. In mice, the Sst-positive neurons feature small, simple receptive fields with limited branching.[20] In stark contrast, their human and pig CMi counterparts are characterized by enormous receptive fields, sometimes spanning several square centimeters, with nerve terminals that are located deeper within the dermis.[59,60]

This divergence underscores a critical theme in modern neuroscience, i.e., transcriptomic orthology does not guarantee functional equivalence. This principle is not without precedent as a similar phenomenon exists in the neocortex, where in the upper layers of the mouse neocortex, Sst-positive neurons are predominantly Martinotti cells, defined by extensive axonal projections to layer 1. In humans, however, the homologous upper layer SST-positive population is far more diverse, containing many cells with non-Martinotti morphologies, including primate-specialized double bouquet cells—a neuronal type first described in the human cortex by Santiago Ramón y Cajal[61]—with extensive axonal projections into deeper cortical layers.

Returning to the somatosensory system, this functional divergence is mirrored at the molecular level by the species-specific expression of key functional genes. A prominent example is

the nicotinic acetylcholine receptor *CHRNA3*. While recent human datasets show *CHRNA3* is specifically expressed in Sst-positive neurons,[26,29,31] it is not expressed in the orthologous Sst-positive neurons in mice; instead, it marks the distinct CGRP-γ population, which does not innervate the skin.[17,20] Further highlighting this divergence, we did not detect considerable *CHRNA3* expression in any neuronal subtype in our pig datasets. This demonstrates that *CHRNA3* expression within this conserved cell type is not a common mammalian trait but may be a specialization of the primate lineage. These findings suggest that while the core genetic program for this neuron class is maintained across species, its ultimate functional role in the skin—and the specific molecular toolkit it uses—differs significantly between rodents and larger mammals, as mice appear to lack clear cutaneous sleeping nociceptors[17–20,62] whereas pigs do possess such neurons.[22,23] This highlights the importance of using models with closer relevance to human biology to supplement rodent data in translational pain research.

Technical considerations and alternative hypotheses

A subset of CMi-fibers can be activated by intense heating of the skin, typically at ∼48°C,[9] and intracutaneous capsaicin activates nearly all CMi-fibers, suggesting robust expression of *TRPV1*. As expected with 10× Genomics 3′ chemistry, our snRNA-seq read coverage is biased toward the 3′ ends of genes.[38] We observed that some genes, including *SCN10A* and *TRPV1*, exhibit unannotated reads in their 3′ untranslated regions (UTRs), likely due to incomplete annotation in the pig reference transcriptome. Despite this, we detected *TRPV1* transcripts in a significant number of C-OSMR-SST neurons, and we reason that our whole-transcriptome Patch-seq data are less affected by this issue.

In designating fiber types (Aβ, Aδ, C), we relied on gene expression profiles and comparisons with existing large mammal datasets. We acknowledge that distinguishing certain fiber types, such as Aδ from C-fibers, remains challenging owing to overlapping gene expression and species-specific differences.[63] In humans, there might be even peripheral unmyelinated nerve fibers, which gain myelination more centrally as suggested from microneurographic experiences with cold-reactive fibers. The cell type with the highest transcriptomic similarity to C-OSMR-SST is the C-OSMR-GFRA1/2 cluster. However, the latter shows a very negative sinus score and no ADS, arguing against a CMi identity. Furthermore, this subgroup expresses high levels of *PIEZO2* in pigs and humans, suggesting mechano-sensitivity.[64] Given that the OSM-responsive fibers in our microneurography recordings were clearly mechano-insensitive, we can reasonably conclude that they do not belong to the C-OSMR-GFRA1/2 cell type.

Limitations of the study

While our study establishes a comprehensive multi-modal map linking transcriptomic and functional features of CMi-fibers in pigs and humans, certain mechanistic aspects remain to be resolved. For example, although our data suggest that *SCN11A*/Nav1.9 contributes to the distinct electrophysiological properties of CMi-fibers, the precise molecular determinants underlying their unique properties and differential response, compared with CM-fibers, remain unknown. Future work using targeted genetic or pharmacological perturbation will be needed to directly test these candidate mechanisms.

Our transcriptomic analyses are limited by sample size and by the coverage of scRNA-seq and snRNA-seq platforms, particularly in capturing low-abundance transcripts, isoform-specific expression, and rare cell types. Patch-seq characterization was performed on dissociated neurons following culturing, which may alter gene expression patterns by upregulating stress or inflammatory transcripts and downregulating ion channel genes. In addition, large-diameter sensory neurons are more difficult to record and harvest, leading to a sampling bias toward smaller neurons and incomplete representation of A-fiber populations. Nevertheless, by identifying the molecular architecture of human dermal sleeping nociceptors, our work now provides a roadmap for future mechanistic studies of these cells, which were previously impossible because of their unknown identity.

Conclusions

In conclusion, this work shows how a multi-modal peripheral sensory neuron taxonomy can inform the molecular characterization of sensory neuron types relevant to human pathophysiology, including human dermal sleeping nociceptors.

RESOURCE AVAILABILITY

Lead contact

Requests for further information and resources should be directed to and will be fulfilled by the lead contact, Angelika Lampert (alampert@ukaachen.de).

Materials availability

This study did not generate new, unique reagents.

Data and code availability

- All raw gene expression data with detailed metadata supporting the findings of this study are openly available in the Gene Expression Omnibus (GEO) at https://www.ncbi.nlm.nih.gov/geo/ under the GEO accession number GSE263532.
- Integration and analysis code, as well as extracted patch recording features, are available at https://github.com/derekhoward/DRG-patchseq.
- Code for the computational model based on an extension of the Hodgkin-Huxley approach is available at https://github.com/tstiehl/nociceptor.

ACKNOWLEDGMENTS

The authors thank the FlowCore and next generation sequencing core facilities of the Medical Faculty Mannheim at Heidelberg University for their assistance with nuclei sorting and generation of single-nucleus gene expression libraries and sequencing. We also thank Heidi Theis (PRECISE, DZNE, Bonn) for preparation of Patch-seq libraries. The authors thank the organ donors and their families for their enduring gift. The authors thank the Genome Center at The University of Texas at Dallas for the services to support pig DRG spatial sequencing. The graphical abstract was created in BioRender: Haag, N. (2026) https://BioRender.com/vgdxvtc; Figure 2A was created in BioRender: Haag, N. (2026) https://BioRender.com/kph6yg1; Figure 3A was created in BioRender: Haag, N. (2026) https://BioRender.com/yzf88j2; Figure 5A was created in BioRender: Haag, N. (2026) https://BioRender.com/w7sple1; Figure 5D was created in BioRender: Haag, N. (2026) https://BioRender.com/kc7kbgw. The authors gratefully acknowledge the following support and funding: Clinician Scientist Program of the Faculty of Medicine of the RWTH Aachen University (J.K.); DFG, German Research Foundation 363055819/GRK2415 (A.L.); DFG, German Research Foundation 368482240/GRK2416 (A.L.); DFG, German Research Foundation

LA 2740/6-1 (A.L.); DFG, German Research Foundation NA 970/7-1 (B.N.); DFG, German Research Foundation 350193106/FOR2690 (B.N.); DFG, German Research Foundation NA 970/9-2 (B.N.); DFG, German Research Foundation 255156212/CRC1158/Z02-INF (H.J.S.); DFG, German Research Foundation 350193106/FOR2690/TP01 (H.J.S.); DFG, German Research Foundation 255156212/SFB1158 A01 (M.S.); DFG, German Research Foundation 350193106/FOR2690 (M.S.); DFG, German Research Foundation KU 1587/10-1 (I.K.); DFG, German Research Foundation KU 1587/11-1 (I.K.); Interdisciplinary Center for Clinical Research within the Faculty of Medicine at the RWTH Aachen University IZKF TN1-1/IA 532001 (A.L.); CAMH Discovery Fund, Krembil Foundation, Kavli Foundation, McLaughlin Foundation, Natural Sciences and Engineering Research Council of Canada (RGPIN-2020-05834 and DGECR-2020-00048) (D.H. and S.T.); Canadian Institutes of Health Research (NGN-171423 and PJT-175254) (D.H. and S.T.); Simons Foundation Autism Research Initiative (D.H. and S.T.); Baden-Württemberg through bwHPC, and the German Research Foundation (DFG) through grant INST 35/1597-1 FUGG (H.J.S. and M.S.); NIH grant U19NS130608 (T.P.); German Research Foundation (DFG) through grant INST 35/1503-1 FUGG (H.J.S. and M.S.); the Interdisciplinary Center for Clinical Research within the faculty of Medicine at the RWTH Aachen University (B.N.); Rotation and START program of the Faculty of Medicine of the RWTH Aachen University (E.E.); and NIH U19 NS130617, Rita Allen Foundation, and Burroughs Wellcome Fund Career Award in Medical Sciences (W.R.). This work was also supported by the Ministry of Culture and Science of North Rhine-Westphalia. NGS analyses were carried out at the Joint Scientific Facility WGGC-PRECISE.

AUTHOR CONTRIBUTIONS

Conceptualization, J.K., D.H., H.J.S., I.K., T.J.P., M.S., B.N., S.T., and A.L.; methodology, J.K., D.H., H.J.S., M.M.M., N.H., I.T., E.E., M.D.B., B.N., S.T., A.L., and T.S.; software, J.K., D.H., M.M.M., D.T.-F., N.N.I., and T.S.; validation, J.K., D.H., H.J.S., S.T., and A.L.; formal analysis, J.K., D.H., H.J.S., M.M.M., A.F., D.T.-F., A.M., J.T., S.A.B., J.S., and B.N.; investigation, J.K., H.J.S., M.M.M., N.H., A.F., A.M., I.T., R.A.B., I.S., D.T.-F., S.S., E.E., L.B., J.S.-S., I.K., J.S., M.S., B.N., S.T., and T.S.; resources, D.T.-F., L.E., M.D.B., B.N., and A.L.; data curation, J.K., D.H., H.J.S., M.M.M., A.F., A.M., M.D.B., J.S., B.N., S.T., and A.L.; writing – original draft, J.K., D.H., M.M.M., T.P., S.T., and A.L.; writing – review and editing, J.K., D.H., H.J.S., M.M.M., N.H., A.F., A.M., E.E., L.E., M.D.B., I.K., M.S., S.A.B., W.R., B.N., S.T., and A.L.; visualization, J.K., D.H., H.J.S., M.M.M., N.H., and S.T.; supervision, M.D.B., T.P., B.N., S.T., and A.L.; project administration, J.K., H.J.S., M.D.B., N.H., T.P., S.T., and A.L.; and funding acquisition, J.K., H.J.S., I.K., W.R., T.P., B.N., and A.L.

DECLARATION OF INTERESTS

A.L. and T.J.P. receive counseling fees from and had research contracts with Grunenthal. W.R. received counseling fees from Grunenthal and has a research contract from Pfizer. Parts of the data in the manuscript (costs for consumables, services, and salary for sequencing Visium spatial transcriptomics and parts of the Patch-seq experiments) were generated within a research contract with Grunenthal. B.N. has a counseling contract with Vertex.

DECLARATION OF GENERATIVE AI AND AI-ASSISTED TECHNOLOGIES IN THE WRITING PROCESS

During the preparation of this work, the authors used ChatGPT and Gemini in order to improve the readability and language of the manuscript. After using this tool, the authors reviewed and edited the content as needed, and they take full responsibility for the content of the published article.

STAR★METHODS

Detailed methods are provided in the online version of this paper and include the following:

SUPPLEMENTAL INFORMATION

Supplemental information can be found online at https://doi.org/10.1016/j.cell.2025.12.048.

Received: October 31, 2024
Revised: August 29, 2025
Accepted: December 22, 2025
Published: February 4, 2026

REFERENCES

1. Kleggetveit, I.P., Namer, B., Schmidt, R., Helås, T., Rückel, M., Ørstavik, K., Schmelz, M., and Jørum, E. (2012). High spontaneous activity of C-nociceptors in painful polyneuropathy. Pain *153*, 2040–2047. https://doi.org/10.1016/j.pain.2012.05.017.
2. Ochoa, J.L., Campero, M., Serra, J., and Bostock, H. (2005). Hyperexcitable polymodal and insensitive nociceptors in painful human neuropathy. Muscle Nerve *32*, 459–472. https://doi.org/10.1002/mus.20367.
3. Sauerstein, K., Liebelt, J., Namer, B., Schmidt, R., Rukwied, R., and Schmelz, M. (2018). Low-Frequency Stimulation of Silent Nociceptors Induces Secondary Mechanical Hyperalgesia in Human Skin. Neuroscience *387*, 4–12. https://doi.org/10.1016/j.neuroscience.2018.03.006.
4. Schmidt, R., Schmelz, M., Torebjörk, H.E., and Handwerker, H.O. (2000). Mechano-insensitive nociceptors encode pain evoked by tonic pressure to human skin. Neuroscience *98*, 793–800. https://doi.org/10.1016/S0306-4522(00)00189-5.
5. Serra, J., Bostock, H., Solà, R., Aleu, J., García, E., Cokic, B., Navarro, X., and Quiles, C. (2012). Microneurographic identification of spontaneous activity in C-nociceptors in neuropathic pain states in humans and rats. Pain *153*, 42–55. https://doi.org/10.1016/j.pain.2011.08.015.
6. Namer, B., and Handwerker, H.O. (2009). Translational nociceptor research as guide to human pain perceptions and pathophysiology. Exp. Brain Res. *196*, 163–172. https://doi.org/10.1007/s00221-009-1777-6.
7. Serra, J., Campero, M., Ochoa, J., and Bostock, H. (1999). Activity-dependent slowing of conduction differentiates functional subtypes of C fibres innervating human skin. J. Physiol. *515*, 799–811. https://doi.org/10.1111/j.1469-7793.1999.799ab.x.
8. Düll, M.M., Riegel, K., Tappenbeck, J., Ries, V., Strupf, M., Fleming, T., Sauer, S.K., and Namer, B. (2019). Methylglyoxal causes pain and hyperalgesia in human through C-fiber activation. Pain *160*, 2497–2507. https://doi.org/10.1097/j.pain.0000000000001644.
9. Schmelz, M., Schmidt, R., Weidner, C., Hilliges, M., Torebjork, H.E., and Handwerker, H.O. (2003). Chemical response pattern of different classes of C-nociceptors to pruritogens and algogens. J. Neurophysiol. *89*, 2441–2448. https://doi.org/10.1152/jn.01139.2002.
10. Schmelz, M., Schmidt, R., Bickel, A., Handwerker, H.O., and Torebjörk, H.E. (1997). Specific C-receptors for itch in human skin. J. Neurosci. *17*, 8003–8008. https://doi.org/10.1523/JNEUROSCI.17-20-08003.1997.

11. Serra, J., Campero, M., Bostock, H., and Ochoa, J. (2004). Two types of C nociceptors in human skin and their behavior in areas of capsaicin-induced secondary hyperalgesia. J. Neurophysiol. *91*, 2770–2781. https://doi.org/10.1152/jn.00565.2003.

12. Obreja, O., Rukwied, R., Nagler, L., Schmidt, M., Schmelz, M., and Namer, B. (2018). Nerve growth factor locally sensitizes nociceptors in human skin. Pain *159*, 416–426. https://doi.org/10.1097/j.pain.0000000000001108.

13. Jonas, R., Namer, B., Stockinger, L., Chisholm, K., Schnakenberg, M., Landmann, G., Kucharczyk, M., Konrad, C., Schmidt, R., Carr, R., et al. (2018). Tuning in C-nociceptors to reveal mechanisms in chronic neuropathic pain. Ann. Neurol. *83*, 945–957. https://doi.org/10.1002/ana.25231.

14. Schmidt, R., Schmelz, M., Forster, C., Ringkamp, M., Torebjörk, E., and Handwerker, H. (1995). Novel classes of responsive and unresponsive C nociceptors in human skin. J. Neurosci. *15*, 333–341. https://doi.org/10.1523/JNEUROSCI.15-01-00333.1995.

15. Weidner, C., Schmelz, M., Schmidt, R., Hansson, B., Handwerker, H.O., and Torebjörk, H.E. (1999). Functional attributes discriminating mechano-insensitive and mechano-responsive C nociceptors in human skin. J. Neurosci. *19*, 10184–10190. https://doi.org/10.1523/JNEUROSCI.19-22-10184.1999.

16. Werland, F., Hirth, M., Rukwied, R., Ringkamp, M., Turnquist, B., Jørum, E., Namer, B., Schmelz, M., and Obreja, O. (2021). Maximum axonal following frequency separates classes of cutaneous unmyelinated nociceptors in the pig. J. Physiol. *599*, 1595–1610. https://doi.org/10.1113/JP280269.

17. Prato, V., Taberner, F.J., Hockley, J.R.F., Callejo, G., Arcourt, A., Tazir, B., Hammer, L., Schad, P., Heppenstall, P.A., Smith, E.S., et al. (2017). Functional and Molecular Characterization of Mechanoinsensitive "Silent" Nociceptors. Cell Rep. *21*, 3102–3115. https://doi.org/10.1016/j.celrep.2017.11.066.

18. Kress, M., Koltzenburg, M., Reeh, P.W., and Handwerker, H.O. (1992). Responsiveness and functional attributes of electrically localized terminals of cutaneous C-fibers in vivo and in vitro. J. Neurophysiol. *68*, 581–595. https://doi.org/10.1152/jn.1992.68.2.581.

19. Handwerker, H.O., Kilo, S., and Reeh, P.W. (1991). Unresponsive afferent nerve fibres in the sural nerve of the rat. J. Physiol. *435*, 229–242. https://doi.org/10.1113/jphysiol.1991.sp018507.

20. Qi, L., Iskols, M., Shi, D., Reddy, P., Walker, C., Lezgiyeva, K., Voisin, T., Pawlak, M., Kuchroo, V.K., Chiu, I.M., et al. (2024). A mouse DRG genetic toolkit reveals morphological and physiological diversity of somatosensory neuron subtypes. Cell *187*, 1508–1526.e16. https://doi.org/10.1016/j.cell.2024.02.006.

21. Middleton, S.J., Barry, A.M., Comini, M., Li, Y., Ray, P.R., Shiers, S., Themistocleous, A.C., Uhelski, M.L., Yang, X., Dougherty, P.M., et al. (2021). Studying human nociceptors: from fundamentals to clinic. Brain *144*, 1312–1335. https://doi.org/10.1093/brain/awab048.

22. Lynn, B., Faulstroh, K., and Pierau, F.K. (1995). The classification and properties of nociceptive afferent units from the skin of the anaesthetized pig. Eur. J. Neurosci. *7*, 431–437. https://doi.org/10.1111/j.1460-9568.1995.tb00339.x.

23. Obreja, O., Ringkamp, M., Namer, B., Forsch, E., Klusch, A., Rukwied, R., Petersen, M., and Schmelz, M. (2010). Patterns of activity-dependent conduction velocity changes differentiate classes of unmyelinated mechano-insensitive afferents including cold nociceptors, in pig and in human. Pain *148*, 59–69. https://doi.org/10.1016/j.pain.2009.10.006.

24. Becker, A.K., Babes, A., Düll, M.M., Khalil, M., Kender, Z., Gröner, J., Namer, B., Reeh, P.W., and Sauer, S.K. (2023). Spontaneous activity of specific C-nociceptor subtypes from diabetic patients and mice: Involvement of reactive dicarbonyl compounds and (sensitized) transient receptor potential channel A1. J. Peripher. Nerv. Syst. *28*, 202–225. https://doi.org/10.1111/jns.12546.

25. Jonas, R., Prato, V., Lechner, S.G., Groen, G., Obreja, O., Werland, F., Rukwied, R., Klusch, A., Petersen, M., Carr, R.W., et al. (2020). TTX-Resistant Sodium Channels Functionally Separate Silent From Polymodal C-nociceptors. Front. Cell. Neurosci. *14*, 13. https://doi.org/10.3389/fncel.2020.00013.

26. Jung, M., Dourado, M., Maksymetz, J., Jacobson, A., Laufer, B.I., Baca, M., Foreman, O., Hackos, D.H., Riol-Blanco, L., and Kaminker, J.S. (2023). Cross-species transcriptomic atlas of dorsal root ganglia reveals species-specific programs for sensory function. Nat. Commun. *14*, 366. https://doi.org/10.1038/s41467-023-36014-0.

27. Kupari, J., Usoskin, D., Parisien, M., Lou, D., Hu, Y., Fatt, M., Lönnerberg, P., Spångberg, M., Eriksson, B., Barkas, N., et al. (2021). Single cell transcriptomics of primate sensory neurons identifies cell types associated with chronic pain. Nat. Commun. *12*, 1510. https://doi.org/10.1038/s41467-021-21725-z.

28. Sharma, N., Flaherty, K., Lezgiyeva, K., Wagner, D.E., Klein, A.M., and Ginty, D.D. (2020). The emergence of transcriptional identity in somatosensory neurons. Nature *577*, 392–398. https://doi.org/10.1038/s41586-019-1900-1.

29. Tavares-Ferreira, D., Shiers, S., Ray, P.R., Wangzhou, A., Jeevakumar, V., Sankaranarayanan, I., Cervantes, A.M., Reese, J.C., Chamessian, A., Copits, B.A., et al. (2022). Spatial transcriptomics of dorsal root ganglia identifies molecular signatures of human nociceptors. Sci. Transl. Med. *14*, eabj8186. https://doi.org/10.1126/scitranslmed.abj8186.

30. Usoskin, D., Furlan, A., Islam, S., Abdo, H., Lönnerberg, P., Lou, D., Hjerling-Leffler, J., Haeggström, J., Kharchenko, O., Kharchenko, P.V., et al. (2015). Unbiased classification of sensory neuron types by large-scale single-cell RNA sequencing. Nat. Neurosci. *18*, 145–153. https://doi.org/10.1038/nn.3881.

31. Nguyen, M.Q., von Buchholtz, L.J., Reker, A.N., Ryba, N.J., and Davidson, S. (2021). Single-nucleus transcriptomic analysis of human dorsal root ganglion neurons. eLife *10*, e71752. https://doi.org/10.7554/eLife.71752.

32. Körner, J., and Lampert, A. (2022). Functional subgroups of rat and human sensory neurons: a systematic review of electrophysiological properties. Pflugers Arch. *474*, 367–385. https://doi.org/10.1007/s00424-021-02656-6.

33. Cadwell, C.R., Palasantza, A., Jiang, X., Berens, P., Deng, Q., Yilmaz, M., Reimer, J., Shen, S., Bethge, M., Tolias, K.F., et al. (2016). Electrophysiological, transcriptomic and morphologic profiling of single neurons using Patch-seq. Nat. Biotechnol. *34*, 199–203. https://doi.org/10.1038/nbt.3445.

34. Gouwens, N.W., Sorensen, S.A., Baftizadeh, F., Budzillo, A., Lee, B.R., Jarsky, T., Alfiler, L., Baker, K., Barkan, E., Berry, K., et al. (2020). Integrated Morphoelectric and Transcriptomic Classification of Cortical GABAergic Cells. Cell *183*, 935–953.e19. https://doi.org/10.1016/j.cell.2020.09.057.

35. Lipovsek, M., Bardy, C., Cadwell, C.R., Hadley, K., Kobak, D., and Tripathy, S.J. (2021). Patch-seq: Past, Present, and Future. J. Neurosci. *41*, 937–946. https://doi.org/10.1523/JNEUROSCI.1653-20.2020.

36. Scala, F., Kobak, D., Shan, S., Bernaerts, Y., Laturnus, S., Cadwell, C.R., Hartmanis, L., Froudarakis, E., Castro, J.R., Tan, Z.H., et al. (2019). Layer 4 of mouse neocortex differs in cell types and circuit organization between sensory areas. Nat. Commun. *10*, 4174. https://doi.org/10.1038/s41467-019-12058-z.

37. Parpaite, T., Brosse, L., Séjourné, N., Laur, A., Mechioukhi, Y., Delmas, P., and Coste, B. (2021). Patch-seq of mouse DRG neurons reveals candidate genes for specific mechanosensory functions. Cell Rep. *37*, 109914. https://doi.org/10.1016/j.celrep.2021.109914.

38. Pool, A.-H., Poldsam, H., Chen, S., Thomson, M., and Oka, Y. (2023). Recovery of missing single-cell RNA-sequencing data with optimized transcriptomic references. Nat. Methods *20*, 1506–1515. https://doi.org/10.1038/s41592-023-02003-w.

39. Renthal, W., Tochitsky, I., Yang, L., Cheng, Y.-C., Li, E., Kawaguchi, R., Geschwind, D.H., and Woolf, C.J. (2020). Transcriptional Reprogramming of Distinct Peripheral Sensory Neuron Subtypes after Axonal Injury. Neuron *108*, 128–144.e9. https://doi.org/10.1016/j.neuron.2020.07.026.

40. Wangzhou, A., McIlvried, L.A., Paige, C., Barragan-Iglesias, P., Shiers, S., Ahmad, A., Guzman, C.A., Dussor, G., Ray, P.R., Gereau, R.W., et al. (2020). Pharmacological target-focused transcriptomic analysis of native vs cultured human and mouse dorsal root ganglia. Pain *161*, 1497–1517. https://doi.org/10.1097/j.pain.0000000000001866.

41. Bhuiyan, S.A., Xu, M., Yang, L., Semizoglou, E., Bhatia, P., Pantaleo, K.I., Tochitsky, I., Jain, A., Erdogan, B., Blair, S., et al. (2024). Harmonized cross-species cell atlases of trigeminal and dorsal root ganglia. Sci. Adv. *10*, eadj9173. https://doi.org/10.1126/sciadv.adj9173.

42. Fischer, S., Crow, M., Harris, B.D., and Gillis, J. (2021). Scaling up reproducible research for single-cell transcriptomics using MetaNeighbor. Nat. Protoc. *16*, 4031–4067. https://doi.org/10.1038/s41596-021-00575-5.

43. Snape, A., Pittaway, J.F., and Baker, M.D. (2010). Excitability parameters and sensitivity to anemone toxin ATX-II in rat small diameter primary sensory neurones discriminated by Griffonia simplicifolia isolectin IB4. J. Physiol. *588*, 125–137. https://doi.org/10.1113/jphysiol.2009.181107.

44. Jones, J., Correll, D.J., Lechner, S.M., Jazic, I., Miao, X., Shaw, D., Simard, C., Osteen, J.D., Hare, B., Beaton, A., et al. (2023). Selective Inhibition of NaV1.8 with VX-548 for Acute Pain. N. Engl. J. Med. *389*, 393–405. https://doi.org/10.1056/NEJMoa2209870.

45. Leipold, E., Liebmann, L., Korenke, G.C., Heinrich, T., Giesselmann, S., Baets, J., Ebbinghaus, M., Goral, R.O., Stödberg, T., Hennings, J.C., et al. (2013). A de novo gain-of-function mutation in SCN11A causes loss of pain perception. Nat. Genet. *45*, 1399–1404. https://doi.org/10.1038/ng.2767.

46. Leipold, E., Hanson-Kahn, A., Frick, M., Gong, P., Bernstein, J.A., Voigt, M., Katona, I., Oliver Goral, R., Altmüller, J., Nürnberg, P., et al. (2015). Cold-aggravated pain in humans caused by a hyperactive NaV1.9 channel mutant. Nat. Commun. *6*, 10049. https://doi.org/10.1038/ncomms10049.

47. Köster, P.A., Leipold, E., Tigerholm, J., Maxion, A., Namer, B., Stiehl, T., and Lampert, A. (2025). Nociceptor sodium channels shape subthreshold phase, upstroke, and shoulder of action potentials. J. Gen. Physiol. *157*, e202313526. https://doi.org/10.1085/jgp.202313526.

48. Tseng, P.-Y., and Hoon, M.A. (2021). Oncostatin M can sensitize sensory neurons in inflammatory pruritus. Sci. Transl. Med. *13*, eabe3037. https://doi.org/10.1126/scitranslmed.abe3037.

49. Lynn, B., Schütterle, S., and Pierau, F.K. (1996). The vasodilator component of neurogenic inflammation is caused by a special subclass of heat-sensitive nociceptors in the skin of the pig. J. Physiol. *494*, 587–593. https://doi.org/10.1113/jphysiol.1996.sp021516.

50. Kankel, J., Obreja, O., Kleggetveit, I.P., Schmidt, R., Jørum, E., Schmelz, M., and Namer, B. (2012). Differential effects of low dose lidocaine on C-fiber classes in humans. J. Pain *13*, 1232–1241. https://doi.org/10.1016/j.jpain.2012.09.008.

51. Cheng, X., Choi, J.-S., Waxman, S.G., and Dib-Hajj, S.D. (2021). Mini-review - Sodium channels and beyond in peripheral nerve disease: Modulation by cytokines and their effector protein kinases. Neurosci. Lett. *741*, 135446. https://doi.org/10.1016/j.neulet.2020.135446.

52. Baker, M.D., and Nassar, M.A. (2020). Painful and painless mutations of SCN9A and SCN11A voltage-gated sodium channels. Pflugers Arch. *472*, 865–880. https://doi.org/10.1007/s00424-020-02419-9.

53. Goodwin, G., and McMahon, S.B. (2021). The physiological function of different voltage-gated sodium channels in pain. Nat. Rev. Neurosci. *22*, 263–274. https://doi.org/10.1038/s41583-021-00444-w.

54. Levy, J.B., Schindler, C., Raz, R., Levy, D.E., Baron, R., and Horowitz, M.C. (1996). Activation of the JAK-STAT signal transduction pathway by oncostatin-M cultured human and mouse osteoblastic cells. Endocrinology *137*, 1159–1165. https://doi.org/10.1210/endo.137.4.8625884.

55. Kwatra, S.G., Bordeaux, Z.A., Parthasarathy, V., Kollhoff, A.L., Alajmi, A., Pritchard, T., Cornman, H.L., Kambala, A., Lee, K.K., Manjunath, J., et al. (2024). Efficacy and Safety of Abrocitinib in Prurigo Nodularis and Chronic Pruritus of Unknown Origin: A Nonrandomized Controlled Trial. JAMA Dermatol. *160*, 717–724. https://doi.org/10.1001/jamadermatol.2024.1464.

56. Szekanecz, Z., Buch, M.H., Charles-Schoeman, C., Galloway, J., Karpouzas, G.A., Kristensen, L.E., Ytterberg, S.R., Hamar, A., and Fleischmann, R. (2024). Efficacy and safety of JAK inhibitors in rheumatoid arthritis: update for the practising clinician. Nat. Rev. Rheumatol. *20*, 101–115. https://doi.org/10.1038/s41584-023-01062-9.

57. Tanaka, Y., Luo, Y., O'Shea, J.J., and Nakayamada, S. (2022). Janus kinase-targeting therapies in rheumatology: a mechanisms-based approach. Nat. Rev. Rheumatol. *18*, 133–145. https://doi.org/10.1038/s41584-021-00726-8.

58. Mwirigi, J.M., Sankaranarayanan, I., Tavares-Ferreira, D., Gabriel, K.A., Palomino, S., Li, Y., Uhelski, M.L., Shiers, S., Franco-Enzástiga, Ú., Wangzhou, A., et al. (2025). Expansion of OSMR expression and signaling in the human dorsal root ganglion links OSM to neuropathic pain. Preprint at bioRxiv. https://doi.org/10.1101/2025.03.26.645611.

59. Namer, B., and Lampert, A. (2025). Functional signatures of human somatosensory C fibers by microneurography. Pain *166*, 2220–2235. https://doi.org/10.1097/j.pain.0000000000003605.

60. Schmidt, R., Schmelz, M., Ringkamp, M., Handwerker, H.O., and Torebjörk, H.E. (1997). Innervation territories of mechanically activated C nociceptor units in human skin. J. Neurophysiol. *78*, 2641–2648. https://doi.org/10.1152/jn.1997.78.5.2641.

61. DeFelipe, J., Ballesteros-Yáñez, I., Inda, M.C., and Muñoz, A. (2006). Double-bouquet cells in the monkey and human cerebral cortex with special reference to areas 17 and 18. Prog. Brain Res. *154*, 15–32. https://doi.org/10.1016/S0079-6123(06)54002-6.

62. Hoffmann, T., De Col, R., Messlinger, K., Reeh, P.W., and Weidner, C. (2015). Mice and rats differ with respect to activity-dependent slowing of conduction velocity in the saphenous peripheral nerve. Neurosci. Lett. *592*, 12–16. https://doi.org/10.1016/j.neulet.2015.02.057.

63. Rostock, C., Schrenk-Siemens, K., Pohle, J., and Siemens, J. (2018). Human vs. Mouse Nociceptors - Similarities and Differences. Neuroscience *387*, 13–27. https://doi.org/10.1016/j.neuroscience.2017.11.047.

64. Coste, B., Mathur, J., Schmidt, M., Earley, T.J., Ranade, S., Petrus, M.J., Dubin, A.E., and Patapoutian, A. (2010). Piezo1 and Piezo2 are essential components of distinct mechanically activated cation channels. Science *330*, 55–60. https://doi.org/10.1126/science.1193270.

65. Ewels, P., Magnusson, M., Lundin, S., and Käller, M. (2016). MultiQC: summarize analysis results for multiple tools and samples in a single report. Bioinformatics. *32*, 3047–3048. https://doi.org/10.1093/bioinformatics/btw354.

66. Grohs, L., Cheng, L., Cönen, S., Haddad, B.G., Bülow, A., Toklucu, I., Ernst, L., Körner, J., Schmalzing, G., Lampert, A., et al. (2023). Diclofenac and other non-steroidal anti-inflammatory drugs (NSAIDs) are competitive antagonists of the human P2X3 receptor. Front. Pharmacol. *14*, 1120360. https://doi.org/10.3389/fphar.2023.1120360.

67. Hirth, M., Rukwied, R., Gromann, A., Turnquist, B., Weinkauf, B., Francke, K., Albrecht, P., Rice, F., Hägglöf, B., Ringkamp, M., et al. (2013). Nerve growth factor induces sensitization of nociceptors without evidence for increased intraepidermal nerve fiber density. Pain *154*, 2500–2511. https://doi.org/10.1016/j.pain.2013.07.036.

68. Ernst, K.J., Okonechnikov, K., Bageritz, J., Mallm, J.-P., Wittmann, A., Maaß, K.K., Leible, S., Boutros, M., Pfister, S.M., Zuckermann, M., et al. (2020). Establishment of a simplified preparation method for single-nucleus RNA-sequencing and its application to long-term frozen tumor tissues. Preprint at bioRxiv. https://doi.org/10.1101/2020.10.23.351809.

69. Yang, L., Tochitsky, I., Woolf, C.J., and Renthal, W. (2021). Isolation of Nuclei from Mouse Dorsal Root Ganglia for Single-nucleus Genomics. Bio Protoc. *11*, e4102. https://doi.org/10.21769/BioProtoc.4102.

70. Turnquist, B., Leverentz, M., and Swanson, E. (2004). Neural spike classification using parallel selection of all algorithm parameters. J. Neurosci. Methods *137*, 291–298. https://doi.org/10.1016/j.jneumeth.2004.02.030.

71. Schmelz, M., Forster, C., Schmidt, R., Ringkamp, M., Handwerker, H.O., and Torebjörk, H.E. (1995). Delayed responses to electrical stimuli reflect

C-fiber responsiveness in human microneurography. Exp. Brain Res. *104*, 331–336. https://doi.org/10.1007/BF00242018.

72. Bretag, A.H. (1969). Synthetic interstitial fluid for isolated mammalian tissue. Life Sci. *8*, 319–329. https://doi.org/10.1016/0024-3205(69)90283-5.

73. Vallbo, A.B., and Hagbarth, K.E. (1968). Activity from skin mechanoreceptors recorded percutaneously in awake human subjects. Exp. Neurol. *21*, 270–289. https://doi.org/10.1016/0014-4886(68)90041-1.

74. Campero, M., Serra, J., Bostock, H., and Ochoa, J.L. (2004). Partial reversal of conduction slowing during repetitive stimulation of single sympathetic efferents in human skin. Acta Physiol. Scand. *182*, 305–311. https://doi.org/10.1111/j.1365-201X.2004.01357.x.

75. Picelli, S., Faridani, O.R., Björklund, A.K., Winberg, G., Sagasser, S., and Sandberg, R. (2014). Full-length RNA-seq from single cells using Smart-seq2. Nat. Protoc. *9*, 171–181. https://doi.org/10.1038/nprot.2014.006.

76. McGinnis, C.S., Murrow, L.M., and Gartner, Z.J. (2019). DoubletFinder: Doublet Detection in Single-Cell RNA Sequencing Data Using Artificial Nearest Neighbors. Cell Syst. *8*, 329–337.e4. https://doi.org/10.1016/j.cels.2019.03.003.

77. Li, C.-L., Li, K.-C., Wu, D., Chen, Y., Luo, H., Zhao, J.-R., Wang, S.-S., Sun, M.-M., Lu, Y.-J., Zhong, Y.-Q., et al. (2016). Somatosensory neuron types identified by high-coverage single-cell RNA-sequencing and functional heterogeneity. Cell Res. *26*, 83–102. https://doi.org/10.1038/cr.2015.149.

78. Nguyen, M.Q., Le Pichon, C.E., and Ryba, N. (2019). Stereotyped transcriptomic transformation of somatosensory neurons in response to injury. eLife *8*, e49679. https://doi.org/10.7554/eLife.49679.

79. Nguyen, M.Q., Wu, Y., Bonilla, L.S., von Buchholtz, L.J., and Ryba, N.J.P. (2017). Diversity amongst trigeminal neurons revealed by high throughput single cell sequencing. PLoS One *12*, e0185543. https://doi.org/10.1371/journal.pone.0185543.

80. Zeisel, A., Hochgerner, H., Lönnerberg, P., Johnsson, A., Memic, F., van der Zwan, J., Häring, M., Braun, E., Borm, L.E., La Manno, G., et al. (2018). Molecular Architecture of the Mouse Nervous System. Cell *174*, 999–1014.e22. https://doi.org/10.1016/j.cell.2018.06.021.

81. Sekerli, M., Del Negro, C.A., Lee, R.H., and Butera, R.J. (2004). Estimating action potential thresholds from neuronal time-series: new metrics and evaluation of methodologies. IEEE Trans. Biomed. Eng. *51*, 1665–1672. https://doi.org/10.1109/TBME.2004.827531.

STAR★METHODS

KEY RESOURCES TABLE

REAGENT or RESOURCE	SOURCE	IDENTIFIER
Antibodies		
Anti-NeuN (Rabbit polyclonal)	Millipore	Cat# ABN78, RRID:AB_10807945
Anti-NeuN-Alexa Fluor 555	Millipore	Cat# MAB377A5, RRID: AB_2814948
Anti-rabbit IgG MicroBeads	Miltenyi Biotec	Cat# 130-048-602, RRID: AB_244362
Chemicals, peptides, and recombinant proteins		
Recombinant human Oncostatin M (carrier free)	R&D Systems/Bio-Techne	Cat# 8475-OM-050/CF
Critical commercial assays		
10X Genomics Visium Spatial Gene Expression Reagent Kit	10X Genomics	PN-1000186
10X Genomics Library Construction Kit	10X Genomics	PN-1000190
10X Genomics Visium Spatial Slide Kit	10X Genomics	PN-1000185
10X Genomics Tissue Optimization Reagent Kit	10X Genomics	PN-1000192
10X Genomics Tissue Optimization Slide Kit	10X Genomics	PN-1000191
Chromium Next GEM Single Cell 3' Kit v3.1	10X Genomics	PN-1000268
Chromium Single Cell Multiome ATAC + Gene Expression Kit	10X Genomics	PN-1000283
Deposited data		
Raw and processed snRNA-seq data	This manuscript, GEO	GEO: GSE263532
Raw and processed Patch-seq data	This manuscript, GEO	GEO: GSE263532
Raw and processed Visium spatial data	This manuscript, GEO	GEO: GSE263532
Transcriptomic data – processed count files	This manuscript, GitHub repository	https://github.com/derekhoward/DRG-patchseq
Electrophysiological data, extracted features	This manuscript, GitHub repository	https://github.com/derekhoward/DRG-patchseq
Action potential model	This manuscript, GitHub repository	https://github.com/tstiehl/nociceptor
Experimental models: Organisms/strains		
Sus Scrofa domesticus (German Landrace)	This Manuscript	N/A
Software and algorithms		
Cell Ranger v6.0.1	10X Genomics	https://www.10xgenomics.com, RRID: SCR_017344
Space Ranger v1.1	10X Genomics	https://www.10xgenomics.com
Loupe Browser v4.2.0	10X Genomics	https://www.10xgenomics.com, RRID: SCR_018555
Seurat v4.3.0	Satija Lab	https://satijalab.org/seurat/, RRID: SCR_016341
MetaNeighbor v1.16.0	Gillis Lab	https://github.com/gillislab/MetaNeighbor-Protocol
limma-voom	Bioconductor	https://bioconductor.org/packages/limma
glmmTMB	CRAN	https://cran.r-project.org/package=glmmTMB
lmerTest	CRAN	https://cran.r-project.org/package=lmerTest
Emmeans	CRAN	https://cran.r-project.org/package=emmeans
R v4.2.2 / RStudio v2022.12.0	R Foundation	https://www.r-project.org, RRID: SCR_001905
Python v3.8 (Anaconda)	Anaconda, Inc.	https://www.anaconda.com, RRID: SCR_008394
Kallisto v0.440	Pachter Lab	https://pachterlab.github.io/kallisto
MultiQC v1.5	Ewels et al.[65]	https://multiqc.info
bcl2fastq2 v2.20	Illumina	https://support.illumina.com
DAPSYS	Brian Turnquist	http://dapsys.net

(*Continued on next page*)

Continued

REAGENT or RESOURCE	SOURCE	IDENTIFIER
QTRAC	Institute of Neurology, UK	https://www.physiol.ucl.ac.uk/research/julianq/qtracp.html
Cellsens Imaging Software	Olympus	https://www.olympus-lifescience.com, RRID: SCR_014551
HEKA PatchMaster / FitMaster	HEKA Electronics	https://www.heka.com

EXPERIMENTAL MODEL AND STUDY PARTICIPANT DETAILS

Pig models

Pigs for Patch-seq

Dorsal root ganglia (DRG) of pigs used for Patch-seq were sampled according to the 3R criteria for reductions in animal use, as leftovers from previous independent animal studies (e.g. LANUV reference no. 81-02.04.2018.A051). For this purpose, 10 female pigs of the German Landrace breed (*Sus scrofa*, German Landrace, wild type, no backcrossing), with an average age of 4.5 month and weight of 47.4 kg (SD 5.2 kg) were euthanized either using an overdose of pentobarbital 60 mg/kg body weight or combination of exsanguination in deep anaesthesia and overdose. No additional housing, feeding, or experimental care was conducted for these animals, as tissue was collected from animals euthanized in independent studies. No experimental group comparisons were made.

Pigs for spatial sequencing

22 fresh-frozen DRG from the lumbar region of 7 female pigs (*Sus scrofa*, German Landrace, wild type, no backcrossing) were used for spatial sequencing. The animals were 14–17 weeks old and weighed 38–55 kg. Euthanasia was performed either by administration of pentobarbital at 60 mg/kg body weight or by exsanguination under deep anaesthesia followed by overdose. Tissues were obtained from animals euthanized as part of unrelated studies, and no additional housing, feeding, or experimental interventions were carried out. No experimental group comparisons were performed.

Pigs for snRNA-seq and in vivo recordings

Experiments were performed on male pigs (*Sus scrofa*, German Landrace, wild type, no backcrossing), aged 10–14 weeks (adolescent stage) and weighing 20–25 kg. Only visibly healthy animals, assessed as fit for transportation from a local licensed livestock facility, were included in the study; no specific pathogen-free or serological screening was performed. All animals were drug- and test-naïve and had no history of prior experimental procedures. Pigs were not housed in the experimental facility prior to the recordings but were delivered from a local licensed livestock facility on the day of experimentation. Thus, no in-house housing, feeding, or temperature control conditions applied. No experimental group comparisons were made; recordings from different fibre classes were obtained across a total of 17 animals. Allocation to experimental conditions was not required, as all animals were subjected to the same in vivo recording procedures. At the end of the experiment, animals were euthanized by intravenous injection of 10 ml Tanax (T-61, Intervet Deutschland GmbH, Unterschleißheim, Germany). Death was confirmed by the induction of lasting electrical silence on the electrocardiogram (ECG) and disappearance of the carotid pulse. All experimental procedures were conducted in accordance with institutional and national guidelines for the care and use of laboratory animals and were approved by the Regierungspräsidium Karlsruhe (Baden-Württemberg, Germany; approval number G-78/18). All procedures conformed to the regulations and ethical standards specified in the approved protocol.

Sex as a biological variable in pigs

For the pig datasets, sex was not systematically varied or analysed. Female pigs were used for Patch-seq and Spatial Sequencing experiments and male pigs for in vivo recordings and snRNA-Seq; this distribution arose from merging independent studies conducted at different centres. No analyses stratified by sex were performed, and potential sex-specific effects on the observed outcomes cannot be excluded. This represents a limitation in the generalizability of the findings.

Human Participants

ADS characterisation cohort

Microneurography experiments for the ADS characterisation were performed in healthy adult volunteers recruited at the University Hospital. A total of 56 participants (27 female, 29 male) were included. Ages ranged from 18–36 years (mean 24.3 years). All participants self-identified as of European ancestry. Volunteers were screened to meet predefined inclusion criteria of being healthy and free of any medication, with the exception of oral contraceptives in female volunteers. No clinical or biological material other than peripheral nerve recordings was obtained. All participants had no history of prior procedures affecting the peripheral nervous system. All recordings were performed in a controlled clinical research environment with standard room temperature. Participants were not assigned to experimental "groups" in the classical sense; instead, single-fiber microneurography recordings were acquired from C-mechanonociceptor (CM) and C-mechano-insensitive nociceptor (CMi) fibers across individuals. A total of 22 CMi fibers and 69 CM fibers were recorded. All procedures were conducted in accordance with institutional and national regulations governing human research. Written informed consent was obtained from all participants prior to the experiments. Microneurography protocols

were approved by the local ethics committee (EK 143/21) and registered in the German Registry for Clinical Studies (DRKS00025261). All procedures conformed to the standards specified in the approved protocol. Experiments were not designed to evaluate sex-dependent differences, and no sex-specific analyses were performed. Potential effects of sex on fiber properties cannot be determined from the current dataset.

OSM characterisation cohort

Microneurography experiments assessing the effects of intradermal OSM injection were performed as self-experiments by seven investigators directly involved in the study. Participants consisted of three female and four male investigators, all Caucasian ancestry, representing a highly educated group with higher socioeconomic status (professors or equivalent). Ages ranged from 34 to 60 (mean 46,9 years). Inclusion criteria required that participants were independent principal investigators or senior researchers contributing to the study and had no history of neuropathic pain or prior procedures affecting peripheral nerve function. No clinical or biological material beyond microneurography recordings was collected. All participants underwent the same injection and microneurography recording protocol. A total of 25 CMi fibers and 35 CM fibers were recorded across the seven self-experimenters. No allocation to experimental groups was performed and single-fiber microneurography recordings were acquired from C-mechanonociceptor (CM) and C-mechano-insensitive nociceptor (CMi) fibers across individuals. Experiments were conducted in a controlled clinical research environment under standard monitoring conditions. Written informed consent for participation and self-administration was obtained from all investigators. Experiments were not designed to evaluate sex-dependent differences, and no sex-specific analyses were performed. Potential effects of sex on fiber properties cannot be determined from the current dataset.

METHOD DETAILS

Study design and oversight

Blinding and power analysis

Patch-seq and sequencing studies did not contain multiple study groups. Hence, the investigators were not blinded during experiments and outcome assessment. There was no predetermination of sample size with statistical methods. In psychophysical and microneurography experiments the volunteers and experimentators were blinded for injection of OSM or control solution. Analyses of psychophysical experiments, flare experiments and microneurography data were performed blinded.

Tissue processing and nuclei isolation

DRG dissociation for Patch-seq

Domestic pigs (German Landrace) DRG from all segments (cervical/thoracic/lumbar) were dissociated according to a procedure described previously.[66] To this end, DRG were transferred on ice and fine excision was performed in ice-cold DMEM F12 medium containing 10% FBS. DRG were treated with 1 mg/ml collagenase P, 1 mg/ml trypsin T1426 and 0,1 mg/ml DNase for digestion. DRG were cut into small pieces inside the digestion medium for surface enlargement. DRG were incubated in 37°C, 5% CO_2 for 120 minutes ± 30 minutes. Approximately after 60 minutes in digestion medium, DRG were triturated using a plastic pipette. Upon completion of the full incubation time, DRG were triturated three times using glass pipettes with decreasing tip diameter. For further purification, DRG were centrifuged at 500 x G and 4°C twice for four minutes each and the pellets were suspended in DMEM F12 with 10% FBS. DRG were subsequently separated from the lighter cell fragments and myelin by centrifugation of a Percoll gradient (containing a 60% Percoll and a 25% Percoll gradient) for 20 minutes at 500 x G. DRG neurons were plated on coverslips coated with poly-D-lysine (100 μg/ml), laminin (10 μg/ml) and fibronectin (10 μg/ml). Neurons were cultured in Neurobasal A medium supplemented with B27, penicillin, streptomycin and L-glutamine and used for voltage-clamp recordings after 12-72 hours in culture. Cells were stored at 37°C, 5% CO_2. We avoided the use of recombinant NGF, as it has been described to decrease the fraction of mechano-insensitive fibers and reduce the magnitude of activity-dependent slowing (ADS) in these fibers.[17,67]

snRNA-Seq nuclei isolation

Male domestic pigs (German Landrace) were euthanized according to ethical approval obtained from the local authorities (RP Karlsruhe, Germany) under the approval number G-78/18. Subsequently, for all five replicates, thoracic and lumbar DRG were quickly dissected, washed once in PBS and stored overnight in RNAlater® at 4°C. 12-16 hours after euthanasia, adjacent fat tissue, the nerve root, and the spinal nerve were trimmed from the DRG under a dissecting microscope. The cleaned DRG were flash-frozen in liquid nitrogen and stored at -80°C until use for nuclei isolation. Nuclei were isolated from 80 mg thoracic and lumbar DRG tissue per sample using one of three previously published protocols, depending on the replicate.[31,68,69]

Replicate 1 followed the protocol of Nguyen et al.[31] In detail, frozen tissue was pulverized and dounced in 1 ml sucrose buffer 1 (in mM: 320 sucrose, 10 HEPES, 5 $CaCl_2$, 3 $MgCl_2$, 0.1 EDTA, 1 DTT; pH 8.0) containing 0.1% Triton X-100 for 10 strokes with the tight pestle. The homogenate was filtered through a 40 μm cell strainer (Greiner) and then centrifuged for 10 min at 3,200 x *g* and 4 °C. The pellet was resuspended in sucrose buffer 1 and further homogenized with an Ultra-turrax homogenizer (T 10 basic with S10N-5G head, IKA). The nuclei were separated from debris by centrifugation (20 min at 3,200 x *g* and 4 °C) through a sucrose density cushion (in mM: 1 sucrose, 10 HEPES, 3 $MgCl_2$, 1 DTT; pH 8.0). The resulting pellet was resuspended in 0.5 ml PBS/1% BSA and subjected to magnetic-assisted neuron enrichment over LS columns (Miltenyi Biotec) using the manufacturer's instructions. To this end, positive selection of neurons was achieved using rabbit polyclonal anti-NeuN antibody (Millipore, cat# ABN78, dilution 1:5,000) and anti-rabbit IgG microbeads (Miltenyi Biotech, cat# 130-048-602, dilution 1:5). The column's eluate was centrifuged

for 8 min at 800 x *g* and 4 °C before the pellet was resuspended in an appropriate volume of resuspension buffer (PBS containing 1% BSA and 0.2 U/μl RNAsin plus [Promega] to reach an approximate nuclei concentration of 1,000/μl.

Replicates 2+3 followed the protocol of Ernst et al.[68] In detail, frozen tissue was pulverized and dounced in 2 ml sucrose buffer 2 (in mM: 320 sucrose, 5 $CaCl_2$, 3 MgAcetate, 2 EDTA, 0.5 EGTA, 10 Tris-HCl, pH 8.0) containing 0.1% Triton X-100 and 1 mM DTT for 10 strokes each, first with the loose and second with the tight pestle. The homogenate was filtered through a stacked 100/40 μm cell strainer combination (both Greiner) and then centrifuged for 5 min at 500 x *g* and 4 °C. After two washes in 5 ml sucrose buffer 2 with the same centrifugation settings, nuclei were resuspended in 0.5 ml PBS/1% BSA/0.2 U/μl RNAsin plus (Promega) and subjected to FACS-based neuron enrichment. For this purpose, the nuclei were stained with Anti-NeuN-Alexa Fluor 555 (Millipore, cat# MAB377A5, dilution 1:100) for 30 minutes at 4°C on a rotator and subsequently with DAPI for 5 minutes on ice. At the FlowCore Mannheim, double-positive singlets were sorted into PBS/1% BSA using a BD FACSAria IIu equipped with a 100 μm nozzle. Sorted neuronal nuclei were washed once in PBS/1% BSA (centrifugation for 5 min at 500 x *g* and 4 °C) and finally resuspended in an appropriate volume of resuspension buffer to reach an approximate nuclei concentration of 1,000/μl.

Replicates 4+5 followed the protocol of Yang et al.[69] In detail, tissue was allowed to thaw on ice in 1 ml homogenization buffer (in mM: 250 sucrose, 25 KCl, 5 $MgCl_2$, 1 DTT, 20 Tricine-KOH, pH 7.8) supplemented with actinomycin (32 μM), BSA (0.04%), and RNAsin plus (0.2 U/μl, Promega) before being cut into small pieces with a scalpel. The tissue pieces were homogenized with an Ultra-turrax homogenizer (see above) and the homogenate was then transferred to a 15-ml dounce homogenizer containing 4 ml homogenization buffer. After 10 strokes with the tight pestle, 320 μl IGEPAL CA-630 (5% v/v in homogenization buffer) was added before 5 more strokes with the tight pestle were conducted. The homogenate was filtered through a 40 μm cell strainer (Greiner) and mixed 1:1 with 50% iodixanol containing the same salt concentrations as the homogenization buffer. Nuclei were then separated from debris by centrifugation (20 min at 10,000 x *g* and 4 °C) through a discontinuous iodixanol gradient consisting of 30% and 40% layers. Nuclei were retrieved from the 30/40% layer interface, washed once with 10 ml PBS/1% BSA (centrifugation for 10 min at 500 x *g* and 4 °C), and finally resuspended in an appropriate volume of resuspension buffer to reach an approximate nuclei concentration of 1,000/μl. All three protocols resulted in similar high-quality nuclei (based on microscopic inspection) and were therefore used as input for microfluidics-based generation of single-nucleus gene expression libraries.

Spatial tissue embedding and fixation

Lumbar DRG from female domestic pigs (German Landrace) were recovered shortly after euthanasia. Tissue was trimmed of fat and connective tissue, rinsed once with artificial cerebrospinal fluid, and freshly frozen in pulverized dry ice. Frozen DRG were stored in a -80°C freezer. For processing, 22 fresh-frozen DRG from the lumbar region of 7 pigs were embedded in optimal cutting temperature (OCT) compound using a cryomold on dry ice. To prevent thawing, OCT was poured in small volumes surrounding the tissue. Two sections of 10 μm thickness were cryosectioned 200 μm apart from each other to ensure distinct neuronal sampling. Sections were mounted onto SuperFrost Plus charged slides for staining with Eosin and Hematoxylin (H&E staining) or onto the capture area of Visium slides for spatial sequencing. Care was taken to avoid tissue folding or overlapping when placing sections onto slides.

Initial tissue quality control was performed using methanol fixation followed by H&E staining, as described in the 10XGenomics Methanol Fixation, H&E Staining & Imaging for Visium Spatial Protocols (Demonstrated Protocol CG000160). We stained a total of 60 sections, each 10 μm in thickness, from 22 fresh frozen DRG. Sections were mounted within the capture areas of 11 Visium slides that contained 55-μm printed barcoded spots. Imaging was conducted using an Olympus vs120 Slide Scanner, utilizing manual load and fluorescence features.

Different permeabilization times (3, 6, 12, 18, 24 and 30 minutes) were evaluated to optimize conditions for gene expression analysis following the 10XGenomics Visium Spatial Gene Expression Reagent Kits - Tissue Optimization User Guide CG000238 Rev E. Reagents were used from the Visium Spatial Tissue Optimization Reagent Kit, PN-1000192 (stored at −20°C) and the Visium Spatial Tissue Optimization Slide Kit PN-1000191 (stored at ambient temperature). Based on the analysis of the tissue optimization, an exposure time of 18 minutes was selected for the permeabilization enzyme.

In vitro electrophysiology

Patch-clamp recording solutions

Extracellular solution contained (in mM): 140 NaCl, 3 KCl, 1 $MgCl_2$, 1 $CaCl_2$, 10 HEPES, 20 glucose (pH 7.4; 300-310 mOsm). Intracellular solution contained (in mM): 4 NaCl, 135 K-gluconate, 3 $MgCl_2$, 5 EGTA, 5 HEPES, 2 Na_2-ATP, 0.3 Na-GTP (pH 7.25; 290-300 mOsm). To minimize RNAse contamination of the intracellular solution (ICS), 100x stock solutions of each component (except ATP and GTP) were made using RNAse-free H_2O or DEPC-treated and autoclaved where appropriate. Afterwards, the final ICS was manufactured by adding GTP, ATP and RNAse free water. Osmolality control was performed.

Patch-clamp recording protocols

Whole-cell patch clamp recordings were performed using a HEKA EPC 10USB amplifier and PatchMaster and analyzed using FitMaster v2.8 software (all HEKA electronics, Lambrecht, Germany). Pipette resistance was 1.5-3.5 MOhm. Currents were low-pass filtered at 10 kHz and sampled at 20 kHz. The liquid-junction-potential was corrected for +14.3 mV. All experiments were performed at room temperature. After reaching giga-seal and pipette capacitance correction, the whole-cell configuration was established. The resting membrane potential (RMP) was measured immediately after establishing the whole-cell configuration. Holding current was then adjusted to achieve a membrane voltage of -60 ± 3 mV.

The sequence of applied pulse protocols was as follows: First, APs were elicited with 200 ms square pulse depolarisations of increasing intensity with an intersweep interval of 5 seconds. Then, 4 Hz sinusoidal and 4 Hz rectangular depolarization pulses were injected with a 5 second break in between to confirm the threshold and compare also longer rectangular threshold with the sinusoidal threshold (sinus_score). The minimum of these pulses was set to Ihold, while the maximum was set to the rheobase. In case this led to no APs due to slight rheobase changes during the recording the maximum was adapted. This was done equally for sinusoidal and rectangular depolarization pulses. This was followed by 20 4 ms rectangular injections of 1000 pA at 2, 5, 10, 25, 50 and 100 Hz for assessment of the maximum follow frequency. Afterwards, the threshold for 500 ms halfsinus-shaped injections was assessed. Finally, a protocol of 75 1000 pA 10 ms rectangular pulses were injected for assessment of changes in slope, membrane potential, AP peak and rising time changes upon repetitive stimulation as a measurement of axonal slowing.[43] The electrophysiological assessment of one cell took around 11 minutes. Following electrophysiological recordings, mRNA were harvested for Patch-seq (see section above for details).

Electrophysiological feature extraction

Electrophysiological feature extraction was performed using in-house scripted IGOR procedures. The first AP evoked by the square pulse protocol was used to calculate the AP properties. The AP threshold was defined as the minimum of the first derivative of the AP (= the point of inflection during the depolarization). The afterhyperpolarization is the minimum after the AP peak. The amplitude is measured between RMP and AP peak. To calculate the AP half-width, half of the voltage between threshold and peak is measured and the time between this voltage point during depolarization and repolarization is evaluated. The time to peak is the duration between current pulse onset and first AP peak. The maximum slope of the upstroke was calculated between threshold and peak, whereas the slope of the subthreshold depolarization was determined between RMP and threshold. Overshoot slope was calculated for the part exceeding 0 mV.

Sine wave affinity (sinus_score) was calculated as the difference in the number of spikes between 20 sinusoidal and 20 rectangular stimulations (theoretical maximum = 20 (20 sinus spikes vs 0 rectangular spikes), theoretical minimum = -20 (0 sinus spikes vs 20 rectangular spikes). Following frequency (FF) is given as the number of spikes elicited by 20 stimulations for each stimulation frequency. Half Sinus Threshold was defined as amount of current injection in which the AP was elicited during half sinus stimulation. Threshold is given relative to AP threshold in the standard rectangular depolarization. Activity-dependent Time to Peak delay was extracted as the change in time to peak in milliseconds compared to the first AP evoked by 75 suprathreshold stimulations. Activity-dependent change in resting membrane potential is given as change in mV of the membrane potential during stimulation compared to potential before stimulation by 75 suprathreshold square voltage pulses. Activity-dependent change in slope is given as maximum in first deviation of AP train normalized to value of first AP evoked by 75 stimulations.

In vivo pig and human experiments

Pig in vivo nerve recordings

All experimental interventions in pigs were approved by the regional ethics council in Karlsruhe, Baden-Wuerttemberg, Germany (G-78/18). *In vivo* extracellular recordings from filaments ''teased'' from saphenous nerves of anesthetized pigs were performed using DAPSYS software (www.dapsys.net).[70] Electrical rectangular pulses (0.5 ms, 20 mA, 0.25 Hz) were delivered by a constant current stimulator (DS7A, Digitimer Ltd., Hertfordshire, UK) via two non-insulated microneurography electrodes (FHC Inc., Bowdoin, ME, USA), inserted intradermally at sites where time-locked APs with C-fiber latencies could be elicited and responsiveness to mechanical stimulation with nylon monofilaments (600 mN; Stoelting, Chicago, IL, USA) was used to classify mechanosensitive polymodal and mechano-insensitive silent nociceptors. Activity-dependent latency increases to electrical stimulation (3 min, 2 Hz) after a 2-minute pause were assessed for both nociceptor classes.[23] At the end of the experiment, pigs were euthanized by i.v. injection of 10 ml Tanax (T-61, Intervet Deutschland GmbH) and death was confirmed by induction of lasting electrical silence on ECG and disappearance of carotid pulse.

Human microneurography (ADS characterization)

APs of single C-fibers from cutaneous C-fiber fascicles of the superficial peroneal nerve were recorded as previously described.[10,71] A tungsten recording needle (2 MΩ, Frederick-Haer, Bowdoinham, ME, USA) is inserted and placed close to an unmyelinated afferent nerve fiber bundle. After reaching a stable position, C-unit innervation territories are detected using a pointed electrode (0.5 mm diameter) delivering electrical pulses. In 50 healthy participants 2 Hz stimulation was performed in C-fiber units - identified by their low conduction velocity (< 2 m/s) - for 3 minutes. Part of those data were utilized for comparison to patch clamp data (see Figure 3). For intracutaneous stimulation, a pair of 0.2 mm needle electrodes (Frederick-Haer) was inserted into the receptive field, with low repetition rates delivered by a Digitimer DS7 constant-current stimulator. Signals were amplified, filtered, stored via custom-written microneurography software (DAPSYS, Brian Turnquist, http://dapsys.net), and analyzed offline with DAPSYS and Microsoft Excel. Single C-fibers were distinguished by conduction latency during continuous low-frequency stimulation (0.25 Hz; $\geq$1.5 $\times$ threshold). Unit characterization employed the ''marking technique,'' which measures activity-dependent slowing (ADS)—a decrease in conduction velocity when a fiber conducts multiple APs in quick succession. ADS magnitude correlates with the number of APs conducted in the seconds before the electrically induced AP. Mechanical sensitivity was assessed by repetitive stimulation of receptive fields with von Frey filaments of 22 g (Stoelting, Chicago, IL, USA). Fibers were classified as: CM-fibers: ADS < 5% during an electrical stimulation protocol (20 pulses at 0.125 Hz, 20 pulses at 0.25 Hz, 30 pulses at 0.5 Hz), latency normalization > 43% within 20 s, and a response to < 22 g von Frey stimulation. CMi-fibers: ADS > 5%, latency recovery < 43%, and no mechanical response to 75 g von Frey stimulation.

OSM human psychophysics and microneurography

500 ng recombinant human oncostatin M protein, carrier free (Biotechne, Minneapolis, Minnesota, U.S., REF Number: 8475-OM-050/CF), diluted in 20 μl sterile synthetic interstitial fluid (SIF)[72] was injected intracutaneously into human volunteers, who provided informed consent. The experiments were conducted on independent researchers who are all senior co-authors of this study (self-experiments). SIF contained (in mM) 107.8 NaCl, 3.5 KCl, 1.5 $CaCl_2$, 0.7 $MgSO_4$, 26.2 $NaHCO_3$, 1.7 NaH_2PO_4, 9.6 sodium gluconate, 5.5 glucose, and 7.7 sucrose with a stable pH of 7.4. The test person and the experimentors were blinded towards the applied substances during experiments.

For psychophysics and to assess flare response, in self-experiments 20 μl in SIF diluted 500 ng OSM, 0.01% Histamine, Histamine+OSM or SIF alone as control were intracutaneously injected at the volar forearms of healthy volunteers in a double-blinded approach. Thereafter ratings were assessed verbally every 10 seconds for 15 minutes on a rating scale from 0 (no pain/itch) to 10 (maximally imaginable itch/pain). Simultaneously, 1 h and 24 h after skin injection, vasodilation via Laser speckle (FLIPI2, Moor Instruments Ltd., Devon, United Kingdom with measurement software V2.0) was assessed. Baseline images were taken before and 24 h after the injections. Erythema areas were calculated as those pixels exceeding the mean flux value + 2-fold standard deviation measured in a control area between the injection sites using data moorFLPI-2 software (Review Software V 5.0, Moor Instruments Ltd)). Hyperalgesia was assessed using von Frey filament stimulation and brush stimulation before injections, after injections, 1 h and 24 h after injections.

For microneurography, in self-experiments in seven healthy volunteers recordings were obtained following pre-established methods[7,11,73,74] using a tungsten microelectrode (200 μm shaft diameter, nominal impedance 1 MΩ, FHC, Inc., USA) placed intraneurally into the superficial peroneal nerve at the ankle level. A reference uninsulated tungsten microelectrode was inserted subcutaneously 1-2 cm away from the nerve trunk. The cutaneous receptive field was electrically stimulated using a pair of stainless-steel needle electrodes resting on the skin. Square pulses (500 μs, typically 1.5 - 2.5 mA) were delivered by an insolated constant-current stimulator (DS7, Digitimer Ltd, UK). Signals were amplified using a differential amplifier (Neuro Amp EX, ADInstruments, Australia, bandpass 300-2,500 Hz), fed to a noise eliminator (Hum Bug, Quest Scientific, Canada) and an audio monitor (AM10 audio monitor, Grass Technologies, USA). Signals were digitized with a data acquisition board (National Instruments, USA) at a sampling rate of 20 kHz. Stimulation and recording were controlled by QTRAC software (Institute of Neurology, UK). Time-locked responses with conduction velocities in the C-fiber range, and with adequate signal-to-noise ratio, were tracked and displayed using a raster plot of latency profiles.[7] Subpopulations of peripheral unmyelinated C-nociceptors were identified based on their profile of activity-dependent slowing of conduction velocity (ADS) as mechano-sensitive C-nociceptors (CM) and mechano-insensitive C-nociceptors (CMi), as detailed previously.[7,74] Specifically, the percentage slowing from rest to 0.25 Hz, and from 0.25 Hz to the end of a 3-minute 2 Hz stimulation period, were calculated. C-nociceptor latencies were continuously tracked before, during and following intracutaneous injection of 20 μl with and without 500 ng OSM administration in the receptive field in the skin directly under the stimulation needles. Thus, OSM affected maximally 5 mm of the nerve fibers. Units were constantly stimulated at a 0.25 Hz frequency. Four period of 3-minute 2 Hz stimulation were obtained twice before (∼ -30 and -15 minutes) and at approximately +15, and +30 minutes after dosing. Both the recordings and the analysis were performed under blind conditions. Investigators were only unblinded after all the measures had been obtained from the raw recordings and the resulting database was locked.

Library preparation and sequencing

Patch-seq mRNA harvesting

Immediately following electrophysiological characterization (described in 'Patch-Clamp Recordings'), sample collection was performed using a specific two-pipette procedure adapted for the large size of pig DRG neurons (Figure S1). First, the recording pipette was retracted from the cell under slightly negative pressure and broken into a PCR-tube containing 4 μl of lysis buffer (40 mM Guanidine hydrochloride, 0.1 mM Smart dT30VN primer, 5 mM dNTPs). Subsequently, a second larger pipette, with tip diameter customized to the specific cell's diameter (resistance ∼0.7 MOhm) was used to collect the entire cell. After collection, this pipette was also broken into the same PCR-tube. Samples were immediately frozen on dry ice. Complete and exclusive collection of the cell was documented using the microscope's camera.

Patch-seq library construction

The harvested samples (cell soma and cytosolic contents in lysis buffer) underwent library preparation following the Smart-Seq2 protocol.[75] Briefly, mRNA was reverse transcribed using the anchored oligo-dT primer (Smart dT30VN) and a template-switching oligonucleotide (TSO), followed by full-length cDNA amplification via PCR. Preamplified cDNA was quantified, and the average size distribution was determined via D5000 assay on a TapeStation 4200 system (Agilent). Tagmentation and subsequent next-generation sequencing (NGS) library generation were performed using 200 pg of cDNA. NGS libraries were quantified by High-Sensitivity dsDNA assay on a Qubit (Invitrogen) and the average size distribution was determined via D5000 assay on a TapeStation 4200 system (Agilent). Libraries were equimolarly pooled and sequenced with 75 base pair single-read (SR) chemistry on a NextSeq500 system (using High Output v2 75-cycle chemistry) or NextSeq2000 system (using a P2 or P3 100-cycle flow cell.

snRNA-Seq library construction

Single-nucleus suspensions were processed at the Next Generation Sequencing Core Facility of the Medical Faculty Mannheim (Heidelberg University) using the 10xGenomics Chromium platform. For samples 1–3, libraries were prepared using the Next

GEM Single Cell 3' v3.1 kit; for samples 4–5, the Next GEM Single Cell Multiome ATAC + Gene Expression kit was used according to the manufacturer's instructions. The resulting gene expression libraries were sequenced on an Illumina NextSeq550 system.

Visium spatial library construction

We utilized the Visium Spatial Gene Expression Reagent Kits (16 rxns PN-1000186), Library Construction Kits (16 rxns PN-1000190) and Visium Spatial Gene Expression Slide Kits (16 rxns PN-1000185). The workflow followed the manufacturer's guidelines (User Guide CG000239 Rev F). In brief, the protocol consists of 5-step process, starting with permeabilization and reverse transcription (step 1). The exposure time of the permeabilization enzyme was 18 minutes based on the analysis of the tissue optimization experiment. After second strand synthesis and denaturation (Step 2), the samples were prepared for a full-length cDNA amplification via Polymerase Chain Reaction (PCR) (step 3). Afterwards, a Visium spatial gene expression library was generated (step 4), followed by sequencing (step 5), performed at the Genomics Core facilities of the University of Texas at Dallas. The samples were sequenced using the Illumina NextSeq2000 Sequencing system.

QUANTIFICATION AND STATISTICAL ANALYSIS

General statistical methods

All statistical analyses were conducted using R (version 4.2.1). Non-parametric tests, including the Wilcoxon Rank-Sum Test / Mann-Whitney U Test and Kruskal-Wallis Test, were applied to evaluate median differences in datasets that were not assumed to follow a normal distribution. The Kruskal-Wallis Test was used for comparisons involving two or more independent groups. Welch's t-test was used to compare means between two groups with unequal variances. For analyses involving multiple group comparisons, ANOVA was used to ascertain mean differences, followed by Tukey's Honest Significant Difference (HSD) Test for post-hoc pairwise comparisons to control for multiple testing errors. Specifics regarding the number of observations, p-values, and the tests used are reported in the figure legends or directly in the main text as appropriate. Statistical significance was defined as a p-value < 0.05.

Pig sequencing data processing

Patch-seq data pre-processing

Raw sequencing data were demultiplexed and converted into fastq format using bcl2fastq2 v2.20. Quality control was performed using MultiQC v.1.5 and reads were pseudoaligned to the *Sus scrofa* genome 11.1 (104, Ensembl) via Kalisto v.0.440 using default parameters.[65] Patch-seq cell samples with fewer than 10,000 reads were excluded from downstream analyses.

snRNA-Seq data pre-processing

Sequencer output files were converted into FASTQ format using Cellranger 6.0.1 mkfastq. Using Cellranger 6.0.1 count, reads were then mapped to the pig genome (Sscrofa11.1 with Ensembl 105 annotation). Transcript abundances were quantified using unique molecular identifiers (UMIs) derived from reads uniquely mapping in sense to the transcriptome (including both exons and introns). Following cell calling within Cell Ranger, the cell-gene expression matrix was imported into R (v4.2.2) for analysis using Seurat (v4.3.0.9001). Low-quality nuclei (fewer than 200 detected UMIs) and doublets (identified using DoubletFinder[76]) were filtered out. For each replicate, mitochondrial reads were regressed out during count normalization with "SCTransform" v2.

snRNA-Seq cell type taxonomy (pig)

snRNA-Seq data were integrated across replicates using Seurat's anchor-based integration workflow to generate an integrated data assay. Dimensional reduction was performed via Principal Component Analysis (PCA) on 3,000 variable features. The first 30 principal components were used to visualize nuclei in two dimensions using uniform manifold approximation and projection (UMAP). Similarly, the first 30 principal components were used for cluster analysis setting the resolution parameter of "FindClusters" to 2. Clusters with high percentage of mitochondrial genes or low number of DEGs likely reflect empty droplets and were therefore removed from the dataset. The resulting dataset (16,979 nuclei) was subset to neurons based on the expression of pan-neuronal markers[31] (SNAP25, SCN9A, THY1, TAC1, and RBFOX1). Clustering analysis was repeated on this neuronal subset, identifying 3,000 variable features for subsequent dimensional reduction, projection and clustering using the same parameters as above. This process yielded 18 clusters, three of which were manually merged based on similar marker gene expression. The final 16 clusters were annotated manually based on the presence or absence of conserved marker genes used to distinguish transcriptionally defined sensory neurons in mice,[30,39,77–80] monkey[26,27] and humans.[26,29,31]

Visium spatial RNA-seq analysis

Illumina BCL files were processed using the Space Ranger v1.1 pipeline (10XGenomics) to align FASTQ files with bright-field microscope images and the pig reference transcriptome (Sscofra11.1). The sequencing run yielded an average of ~59 million reads per sample, with 84.2% of reads mapping confidently to the genome. Across the tissue sections, we detected an average of 13,870 unique genes. The pipeline identified an average of 1,574 spatial spots (barcodes) covered by tissue, with a mean sequencing depth of 40,490 reads per spot. Barcoded spots overlapping single neurons were visualized using the Loupe Browser (v4.2.0, 10x Genomics). To prevent double counting, barcodes overlapping multiple neurons were excluded. As a quality control step, neuronal barcodes with fewer than 100 reads and no counts of the neuronal marker *SNAP25* were removed.

Visium morphology and barcode selection

To link transcriptomic data with cell morphology, we followed the approach described by Tavares-Ferreira et al. (2022).[29] Using the Loupe Browser (v4.2.0, 10x Genomics), we manually selected barcoded spots overlapping individual neuronal cell bodies based on

tissue morphology in H&E-stained sections. Positional data (coordinates) of these barcodes were exported, and the corresponding.-tif images were visualized using Cellsens imaging software. We utilized the polyline measuring tool to determine the diameter of neurons exhibiting distinct nuclear staining, ensuring sectioning occurred through the central region of the cell. Measurements were strictly limited to neurons exhibiting distinct nuclear staining (confirming sectioning through the cell center) and lacking freezing artifacts. To ensure high-quality, neuron-specific data, we excluded barcodes overlapping multiple neurons, retaining only those overlapping single, clearly identifiable neurons.

RNA-Seq dataset integration

Pig cross-dataset cell typing

The pig snRNA-Seq dataset was used as the reference for integrating additional pig datasets (Patch-seq and Visum spatial transcriptomics), ensuring consistent cell type mapping across technologies. The Patch-seq dataset contained 22,259 genes, and the Visium dataset contained 15,924 genes; these were aligned to the snRNA-Seq reference (30,477 genes) using the intersection of gene symbols. Cross-dataset integration was performed using the Canonical Correlation Analysis (CCA) workflow from Seurat (v4.3.0). Patch-seq data were treated as a single batch and integrated with the reference using SCTransform v2 normalization (mitochondrial reads regressed out). We selected 6,000 highly variable genes as integration anchors (SelectIntegrationFeatures). Datasets were integrated using the IntegrateData function with the 'normalization.method' parameter set to "SCT", and 'k.weight' set to 75. Dimensionality reduction was performed via PCA (50 dimensions), and the first 30 principal components were used for UMAP visualization. To assign cell type labels to Patch-seq neurons, we used a K-nearest neighbour (KNN) approach. Neighbors were defined using *FindNeighbors* (first 30 PCs) and identified using *TopNeighbors* (k = 20). Each Patch-seq neuron was assigned the most frequent snRNA-Seq-based cell type found among its 20 nearest neighbours. A similar approach was used for the pig Visium dataset; however, due to the large dataset size, we processed the Visium data in batches (maximum 250 cells per donor) to facilitate the use of identical integration and mapping parameters.

Marker gene identification and correlation

To identify transcriptional markers for each DRG neuron subtype, we performed differential expression analysis using the FindAllMarkers() function from Seurat (v4.3.0) separately for each dataset. Parameters were set to maximize the number of tested genes (min.pct and logfc.threshold to -Inf, min.cells.feature and min.cells.group to 1). To determine agreement of transcriptional markers across the datasets, we computed enrichment fold changes (avg_log2FC) for each gene in each cell type relative to all other cells. We intersected the lists of enriched genes between dataset pairs and correlated their enrichment values using Spearman's correlation (cor.test in R).

Cross-species cell type replicability

We assessed cell type replicability between our pig snRNA-Seq dataset and cross-species DRG atlases from Bhuiyan et al. (2024)[41] and Qi et al. (2024)[20] using two complementary approaches: MetaNeighbor for cell type replicability assessment and Seurat's label transfer for cell type prediction. MetaNeighbor (version 1.16.0) was used to assess cell type replicability between our pig snRNA-Seq data and the cross-species atlas.[42] This unsupervised method quantifies cell type similarity based on the correlation of gene expression patterns among neighbors. We identified 1,172 highly variable genes (variableGenes) and used MetaNeighborUS (one_vs_best = TRUE, symmetric_output = FALSE) to generate a cell-cell similarity network. Replicability was quantified as the area under the receiver operator characteristic curve (AUROC). Results were visualized as a cluster graph using makeClusterGraph (low_threshold = 0.3) and plotClusterGraph. To predict cell types for our pig snRNA-Seq data using the cross-species atlas as reference, we used Seurat's label transfer workflow (version 4.3.0.1). Pig data were preprocessed (normalization, feature selection, scaling, PCA) and anchors were identified between the pig query and the cross-species reference using FindTransferAnchors (assay = "RNA", reduction = "cca"). Cell type labels were transferred using TransferData, and the pig data were projected onto the reference UMAP space using MapQuery for visualization.

Computational analyses and integration

Principal Component Analysis (PCA) of Electrophysiological Features, CMi phenotype and expression analysis

To generate a composite score for the CMi-like phenotype, we performed Principal Component Analysis (PCA) on four key electrophysiological features from 226 patch-clamp recorded neurons: action potential duration (APD), response to 50 Hz stimulation, sinus score, and relative activity-dependent slowing (Rel. ADS). Missing values were imputed using a k-nearest neighbor (k=5) approach, prior to scaling and centering. PCA was performed using the prcomp function in R. The first principle component (PC1) served as the "CMi score". To identify genes associated with the CMi phenotype, we performed differential expression analysis using the limma-voom pipeline. The CMi score (PC1 from the electrophysiological PCA) was used as a continuous variable in the design matrix. Genes were considered significantly differentially expressed if they met an adjusted p-value < 0.05 and absolute log2 fold change > 0.5.

Computational action potential modelling

We used computational modelling to study the impact of SCN11A abundance on the AP morphology. We adapted the modelling framework from[47] to C-OSMR-SST neurons. The model considers SCN1A-5A & 8A-11A and is based on an extension of the Hodgkin-Huxley approach which accounts for non-exponential inactivation kinetics and shows better agreement to data. The gating parameters were fitted based on voltage clamping data and are taken from.[47] The contribution of a given sodium channel subtype to the total sodium conductance is chosen according to its expression level in C-OSMR-SST neurons. The APs were generated by a

current injection of 30μA/cm $^{-2}$ starting at time 0 and lasting until the end of the observation period. The AP width was measured at the threshold voltage which was determined using the second derivative of dV/dt with respect to V as described in [81]. See also Methods S1 for extended information, parameters and deduction of the model.

Modeling of OSM flare and psychophysics

To model the count-based acute Flux Data, we used a generalized linear mixed model (GLMM) with a negative binomial distribution (nbinom2 family, log link) to account for overdispersion, using the glmmTMB package. Fixed effects included Hist, OSM, Time, and all interactions (Hist × OSM × Time), with a random intercept for Subject. For the outcomes Pain and Itch, linear mixed-effects models were fitted using the lmer function from the lmerTest package. Both variables exhibited non-normal distributions and were square root-transformed to meet model assumptions of normality. Each model included fixed effects for Intervention, Time, and their interaction (Intervention × Time), and a random intercept for Subject. Pairwise comparisons of estimated marginal means (EMMs) were performed using the emmeans package, with p-values adjusted for multiple testing using the Bonferroni or Tukey method as appropriate. Estimated contrasts are presented on the response scale, along with 95% confidence intervals. Model assumptions were checked via diagnostic plots of residuals and random effects as well as BIC and AIC comparisons. Specifics regarding the number of observations, p-values, and the tests used are reported in the figure legends or in the supplementary tables.

ADDITIONAL RESOURCES

Registration of the ADS characterization experiments (Microneurography) in the German Registry for Clinical Studies: https://drks.de/search/de/trial/DRKS00025261.

CellPress
OPEN ACCESS

Supplemental figures

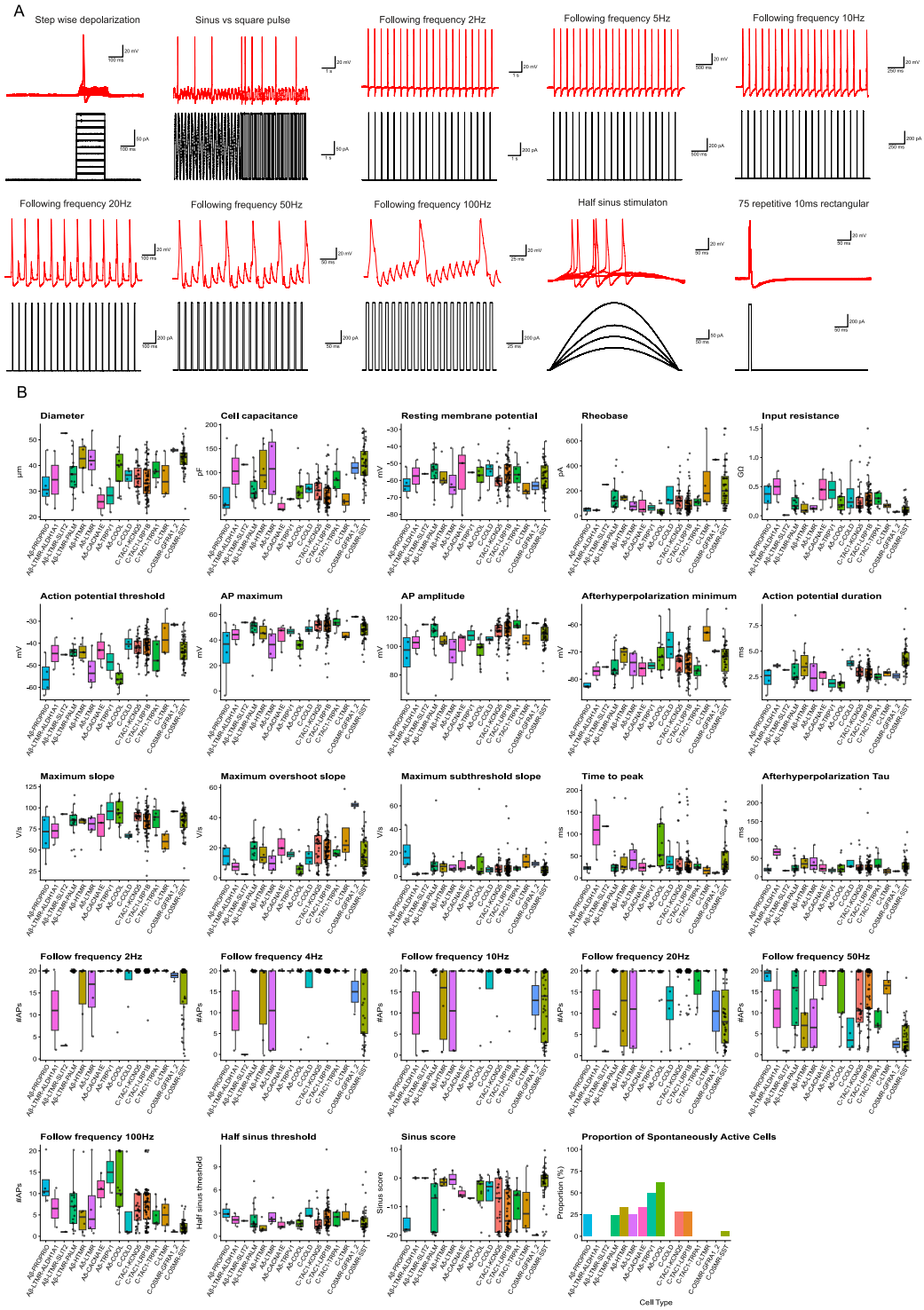

(legend on next page)

Figure S1. Extended electrophysiological data, related to Figure 1

(A) Pulse protocols (black) for electrophysiological assessment and example patch-clamp recording traces of pig DRGs (red). From up left to down right: 200 ms stepwise depolarization protocol; sine vs. rectangular 4 Hz stimulation; 20 1 nA pulses at 2, 5, 10, 20, 50, and 100 Hz; 500 ms half sine-shaped stimulation; 75 repetitive 1 nA 10-ms stimulations.

(B) Combined scatterplot and boxplot showing quantification of each electrophysiological feature per mapped transcriptomic identity.

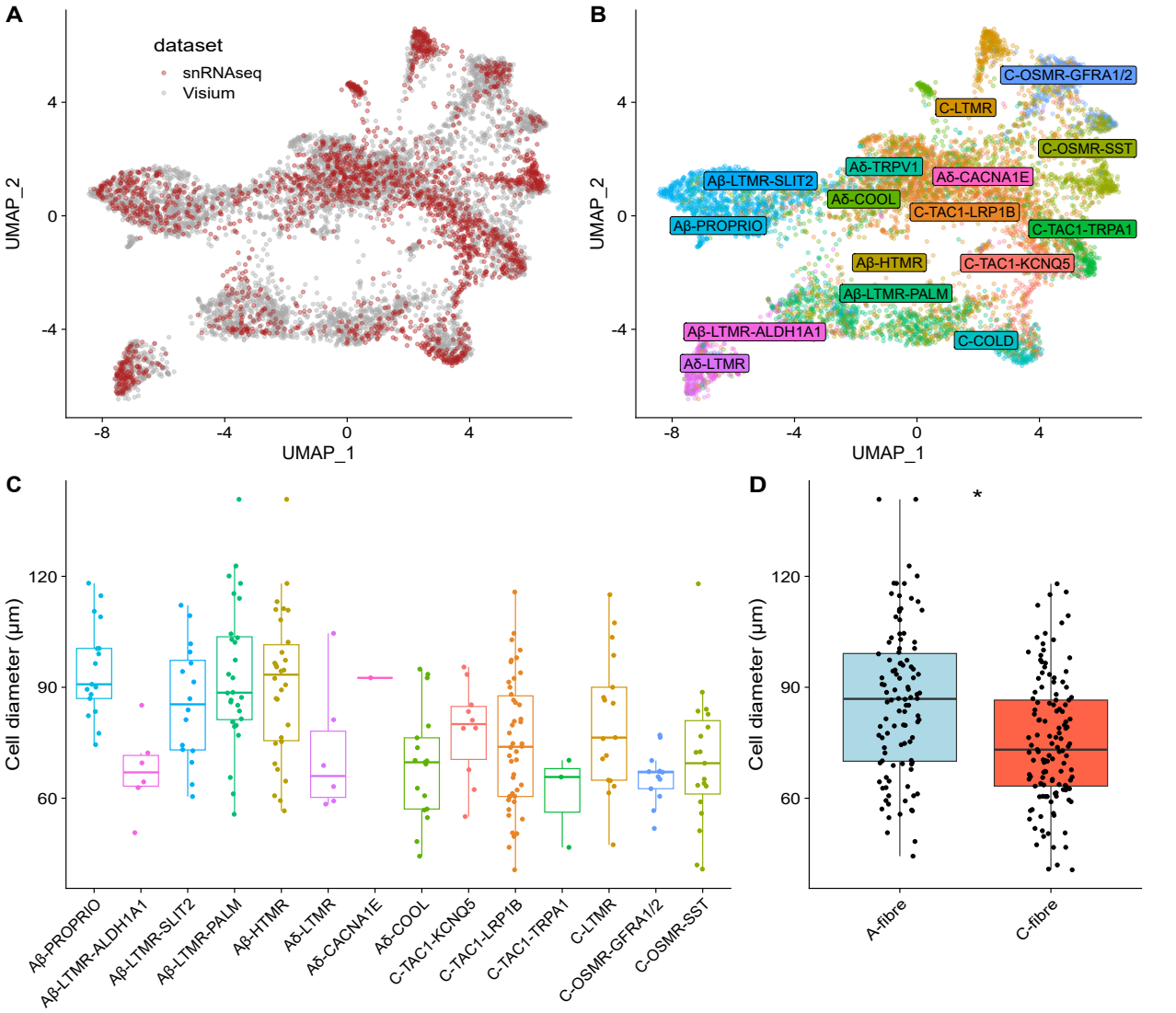

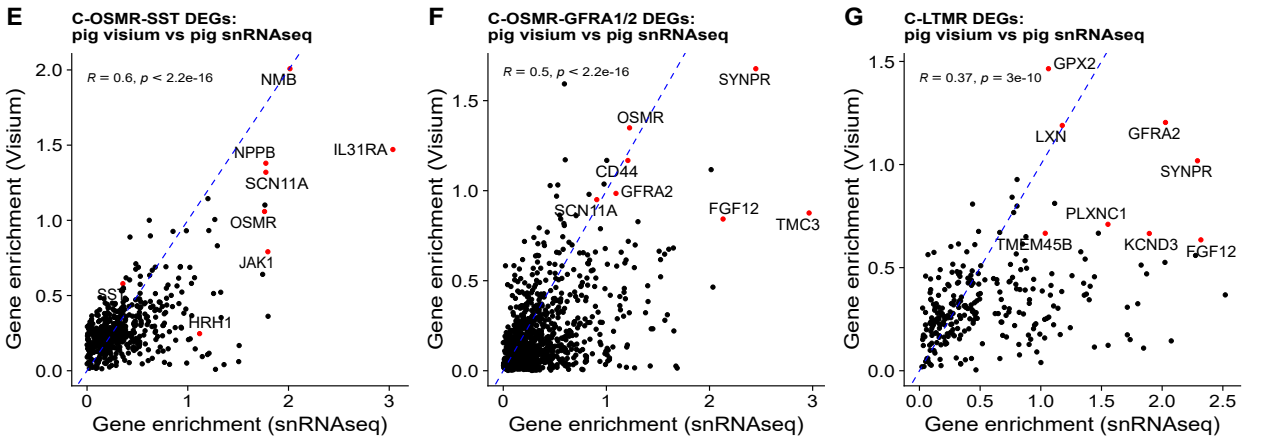

(legend on next page)

Figure S2. Spatial transcriptomics of pig DRGs corroborates cell-type-enriched marker gene expression across technologies, related to Figure 1

(A) UMAP representation of integrated gene expression from snRNA-seq (red) and Visium-based spatial transcriptomics (gray).

(B) Same representation as in (A) but with colors distinguishing the mapped cell types.

(C and D) Cell diameters based on manual quantification of 230 DRG neurons from the Visium dataset illustrated as neuronal subtype (C), and at broad cell-type resolution (85.5 ± 1.9 μm for A-fibers, 73.7 ± 1.6 μm for C-fibers, t = 4.81, df = 226.72, Welch's *t* test $p = 2.72 \times 10^{-6}$, mean ± SEM) (D).

(E–G) Illustration of concordance of cell-type-enriched differential gene expression (DEG) for C-OSMR-SST (E), C-OSMR-GFRA1/2 (F), and C-LTMR cells (G). Each dot reflects a gene, with *x* and *y* axes values indicating $\log_2$ fold changes of enrichment of target cell type (e.g., C-OSMR-SST cells), compared with all other cells in snRNA-seq dataset (*x* axis) and Visium spatial transcriptomics dataset (*y* axis). Genes subset to those with positive enriched expression in both technologies. Inset values indicate Pearson correlations (R) and associated *p* values. Genes denoted in red indicate cell-type markers or otherwise notable genes.

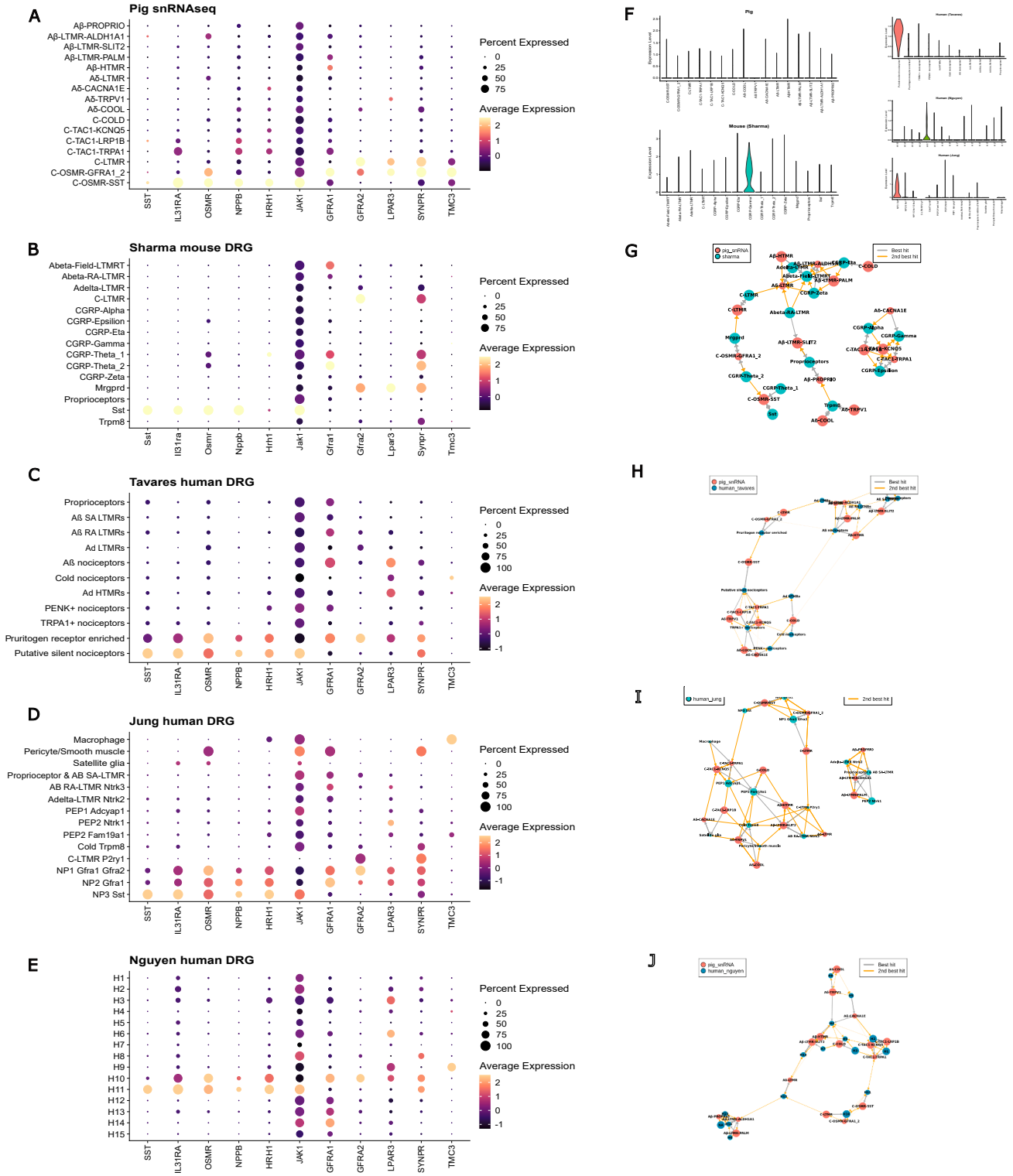

Figure S3. Cross-species DRG transcriptomic cell-type replicability, related to Figure 2

(A–E) Dotplots showing expression of key marker genes for C-OSMR-SST neurons and related cell types across different datasets. The size of each dot represents the percentage of cells expressing the gene, while the color intensity indicates the average expression level. (A) Pig snRNA-seq data collected in this study. (B) Qi et al. mouse toolkit atlas. (C–E) Human DRG data subsets from previously published cross-species atlas: (C) Tavares et al. human DRG dataset, (D) Jung et al. human DRG dataset, and (E) Nguyen et al. human DRG dataset.

(legend continued on next page)

(F) Violin plots showing expression of CHRNA3 across datasets included for comparison. While CHRNA3 is expressed in the SST+ traits in human datasets, it is expressed in the CGRP-gamma subgroup in mice.
(G–J) MetaNeighbor cluster graphs comparing pig snRNA-seq cell types (red nodes) to human DRG cell types (blue nodes) from different studies in the cross-species atlas. (G) Comparison with Qi et al. from mouse DRG data. (H) Comparison with Tavares et al. human DRG data. (I) Comparison with Jung et al. human DRG data. (J) Comparison with Nguyen et al. human DRG data.

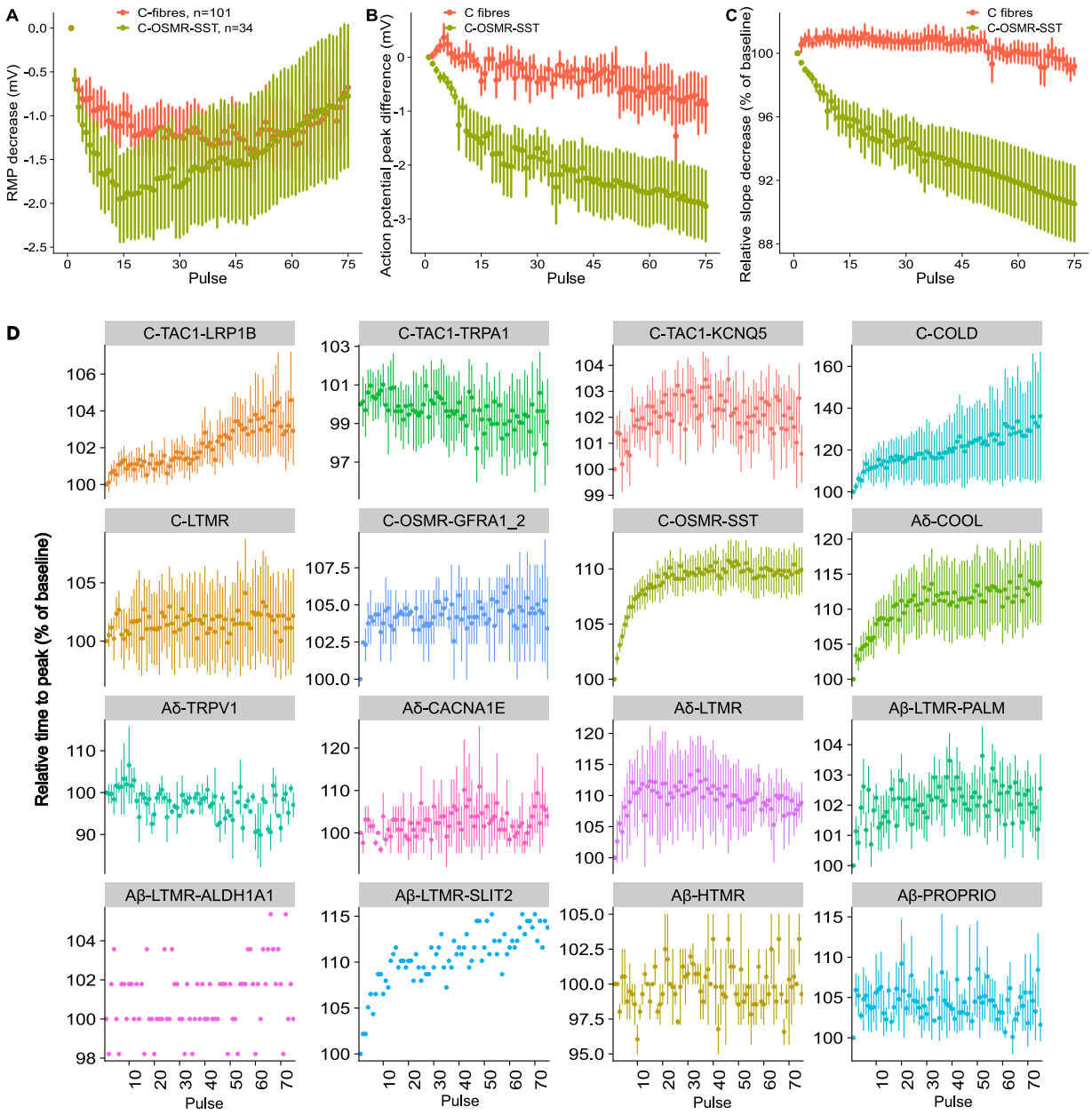

Figure S4. Extended electrophysiological characterization of CMi-fibers, related to Figure 3

Supplemental data on functional biomarkers derived from *in vivo* microneurography experiments.

(A) Relative change in maximum AP slope upon 75 rectangular 1,000 pA stimulations with 10 ms and 2 Hz for C-OSMR-SST cells, compared with all other Patch-seq-characterized C-fiber neurons (mean change 0.906 ± 0.0235 SEM vs. 0.992 ± 0.00586 SEM; Mann-Whitney U = 2,829.5, $p < 1.733 \times 10^{-8}$).

(B) Relative change in maximum AP peak voltage upon 75 rectangular 1,000 pA stimulations with 10 ms and 2 Hz for C-OSMR-SST cells, compared with all other C-fiber neurons (mean change −3.08 ± 0.723 mV vs. −0.877 ± 0.540 mV; Mann-Whitney U = 2589.5, $p < 9.855 \times 10^{-6}$).

(C) Relative change in resting membrane potential upon 75 rectangular 1,000 pA stimulations with 10 ms and 2 Hz for C-OSMR-SST cells, compared with all other C-fiber neurons.

(D) Relative time to peak during 75 rectangular 1,000 pA stimulations with 10 ms and 2 Hz for all cell types in the dataset. Error bars indicate SEM.

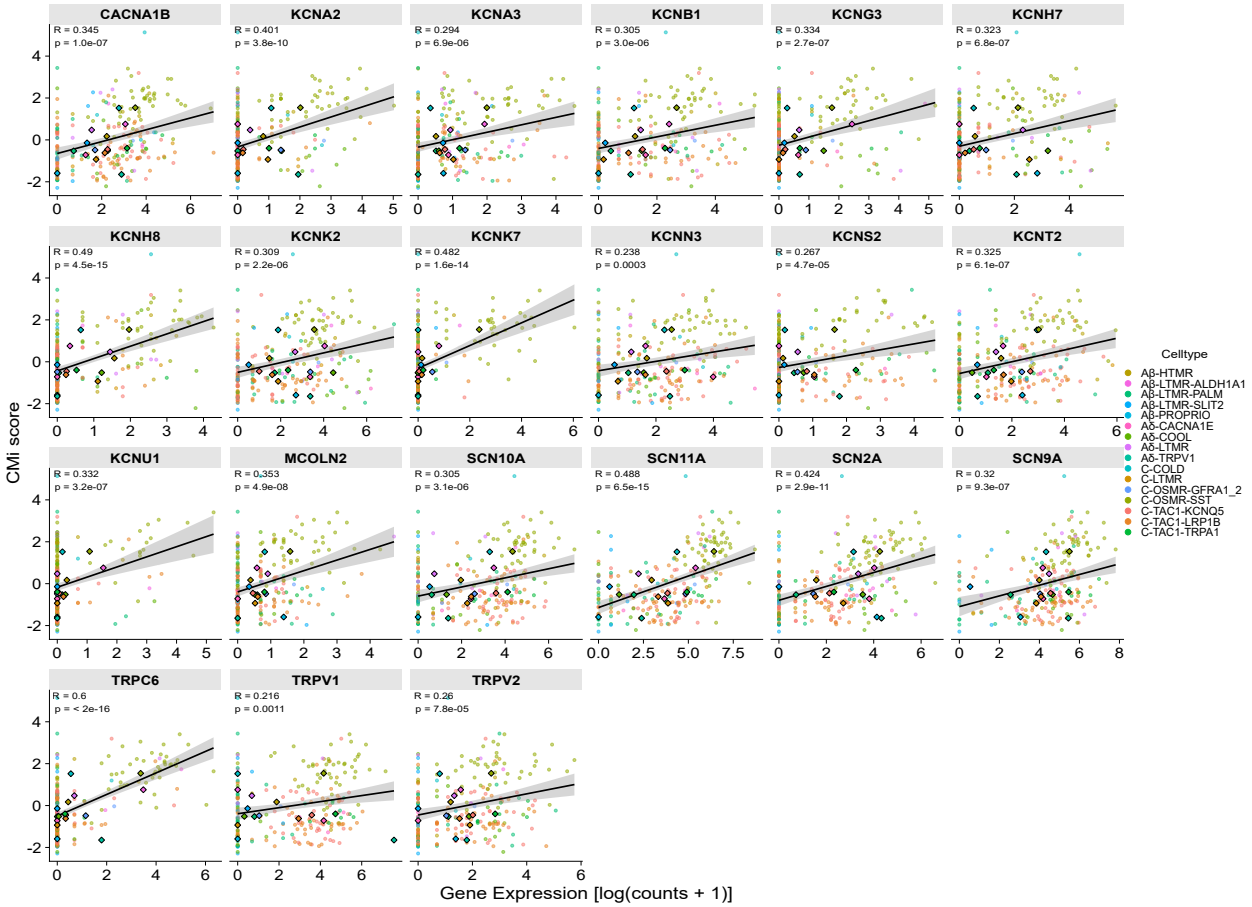

Figure S5. Correlation between ion channel expression and CMi score, related to Figure 4

Correlation between ion channel expression and CMi score. Each point represents a single neuron, colored by cell type. Larger diamond-shaped points indicate the mean expression and CMi score for each cell type. The black line shows linear regression fit with 95% confidence interval.

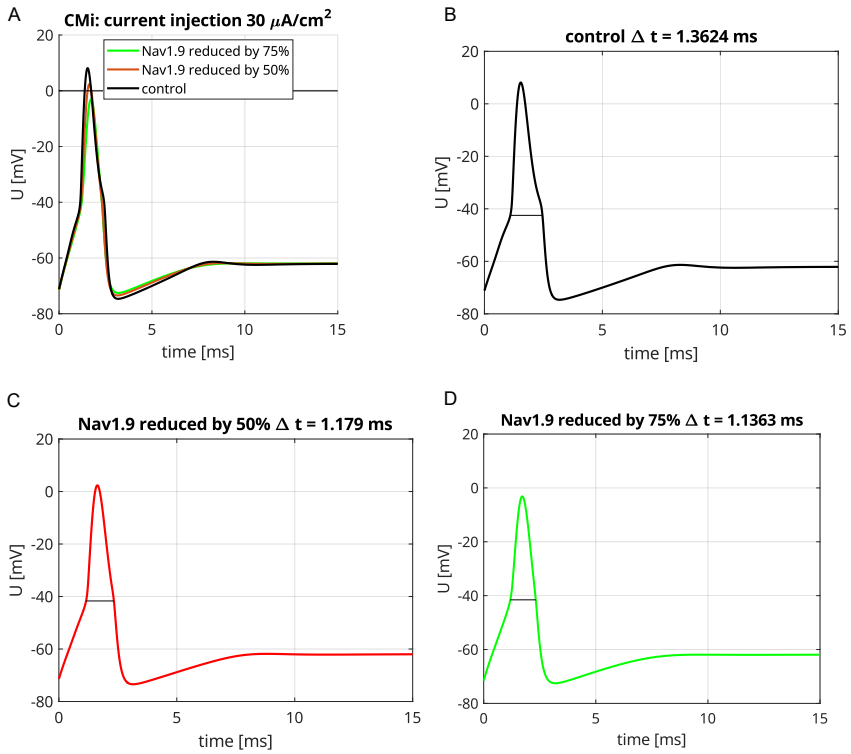

Figure S6. Simulated impact of SCN11A abundance on the AP morphology in C-OSMR-SST neurons, related to Figure 4

(A) Overlay of the three simulated AP with the relative abundance of SCN isoforms corresponding to their gene expression.

(B) The black line (control) shows the simulated AP with the relative abundance of SCN isoforms corresponding to their gene expression.

(C and D) The maximal conductance attributed to SCN11A is stepwisely reduced by 50% (C) (red line) and 75% (D) (green line), compared with the control. The maximal conductances attributed to the other isoforms are increased proportionally to their expression, such that the total maximal sodium conductance remains unchanged. At the beginning of the simulation the neurons are in their resting state. The AP width (Δt) is measured at the threshold voltage and indicted by a horizontal line. Current injection starts at time 0 and lasts until the end of the simulation period. Maximal slopes: (B): 213.4 mV/ms, (C): 152.0 mV/ms, (D): 109.2 mV/ms.

See also Methods S1.

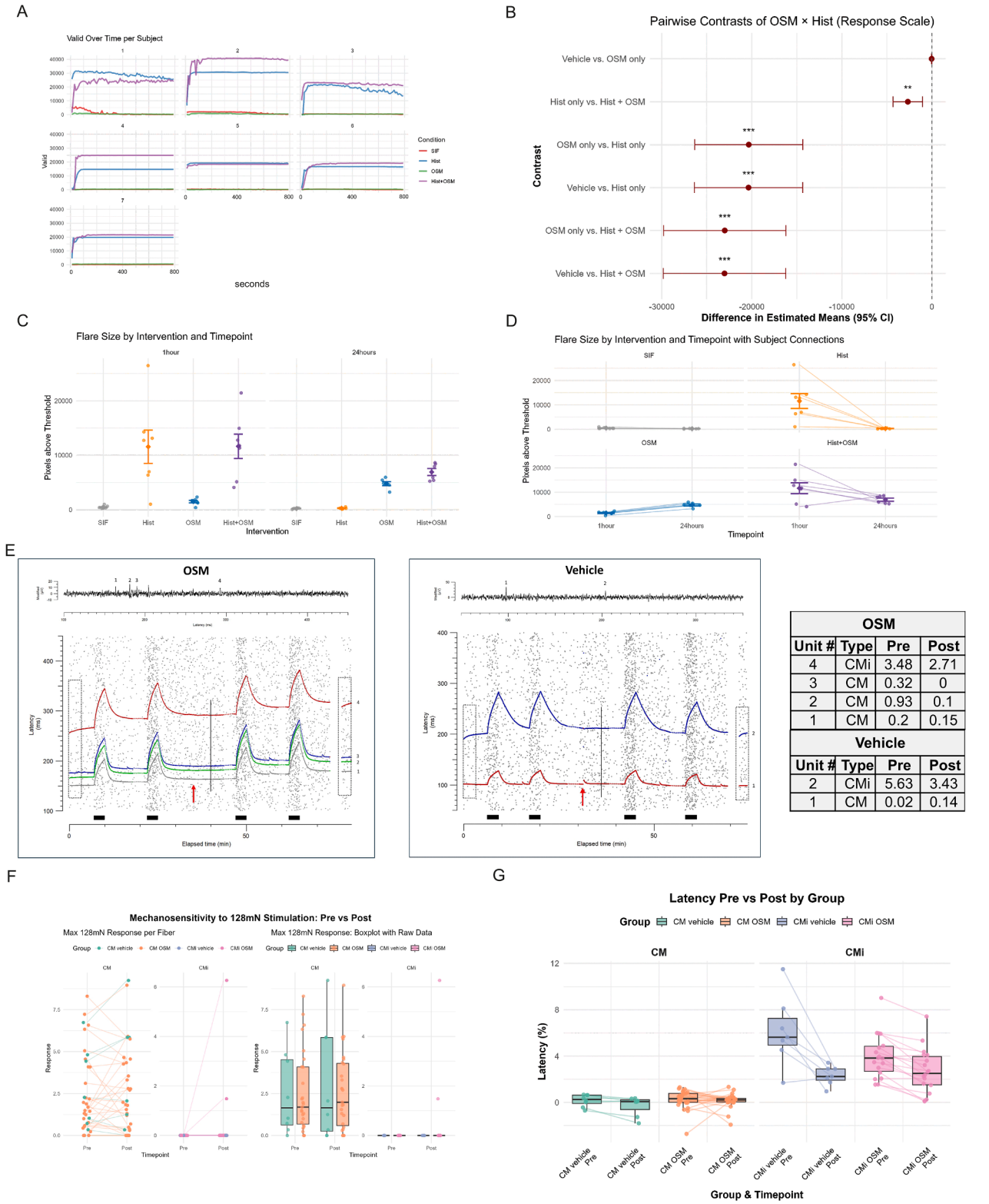

OSM			
Unit #	Type	Pre	Post
4	CMi	3.48	2.71
3	CM	0.32	0
2	CM	0.93	0.1
1	CM	0.2	0.15
Vehicle			
Unit #	Type	Pre	Post
2	CMi	5.63	3.43
1	CM	0.02	0.14

Figure S7. OSM increases acute histamine-evoked axon reflex flare and induces subacute flare independently, related to Figure 5

(A) Flare area quantified over time per subject following intradermal injection of SIF (control), histamine (Hist), OSM, or a combination of histamine and OSM (Hist + OSM). Frame rate: 10 s.

(legend continued on next page)

(B) Pairwise model-based contrasts from a negative binomial generalized linear mixed model (GLMM) indicate significant effects of histamine and OSM, as detailed in Table S2.
(C) Quantification of flare area at 1 and 24 h after injection, showing sustained responses under OSM and Hist + OSM conditions (n = 7 at 1 h; n = 6 at 24 h).
(D) Individual fiber-level changes in flare area at 1 and 24 h, connected per fiber. Statistical details and full model results are provided in Table S2.
(E) Two examples of microneurography recordings from the superficial peroneal nerve before and after blind administration (red arrow) of OSM (left) and vehicle (right) in two different healthy volunteers. Raster plot of latencies showing ADS of conduction velocity when stimulation rate is increased from 0.25 to 2 Hz (filled bars). Several raster latencies are numbered in increasing order from shorter to longer latency and classified as mechano-sensitive (left panel units 1, 2, 3; right panel unit 1) and CMi nociceptors (left panel unit 4; right panel unit 2). At the top of each panel there is an example of a single sweep of the modified neurogram taken at the time of the solid vertical line shown in the raster (note: the neurograms are inverted for better visualization of the predominantly triphasic negative C-fiber AP as an upward deflection). Table shows percentage slowing from 0 to 0.25 Hz pre-dosing at the beginning and post-dosing at the end of the experiment (open dotted boxes).
(F) ADS, assessed as maximum change in latency (%), is shown across fiber types and intervention (vehicle vs. OSM), before and after treatment. Left: individual fiber responses with connecting lines; Right: group-level boxplots. Sample sizes: CM-fibers: n = 8 vehicle, n = 27 OSM; CMi-fibers: n = 7 vehicle, and n = 18 OSM.
(G) Latency change (post – pre) across fiber types and interventions, highlighting OSM-dependent effects on ADS. Sample sizes are the same as in (A). Statistical analyses of MNG data were conducted using a linear mixed-effects model with repeated measures for pre- and post-injection and between-subject factors of OSM treatment and fiber type. Model summaries and pairwise contrasts are provided in Table S3.

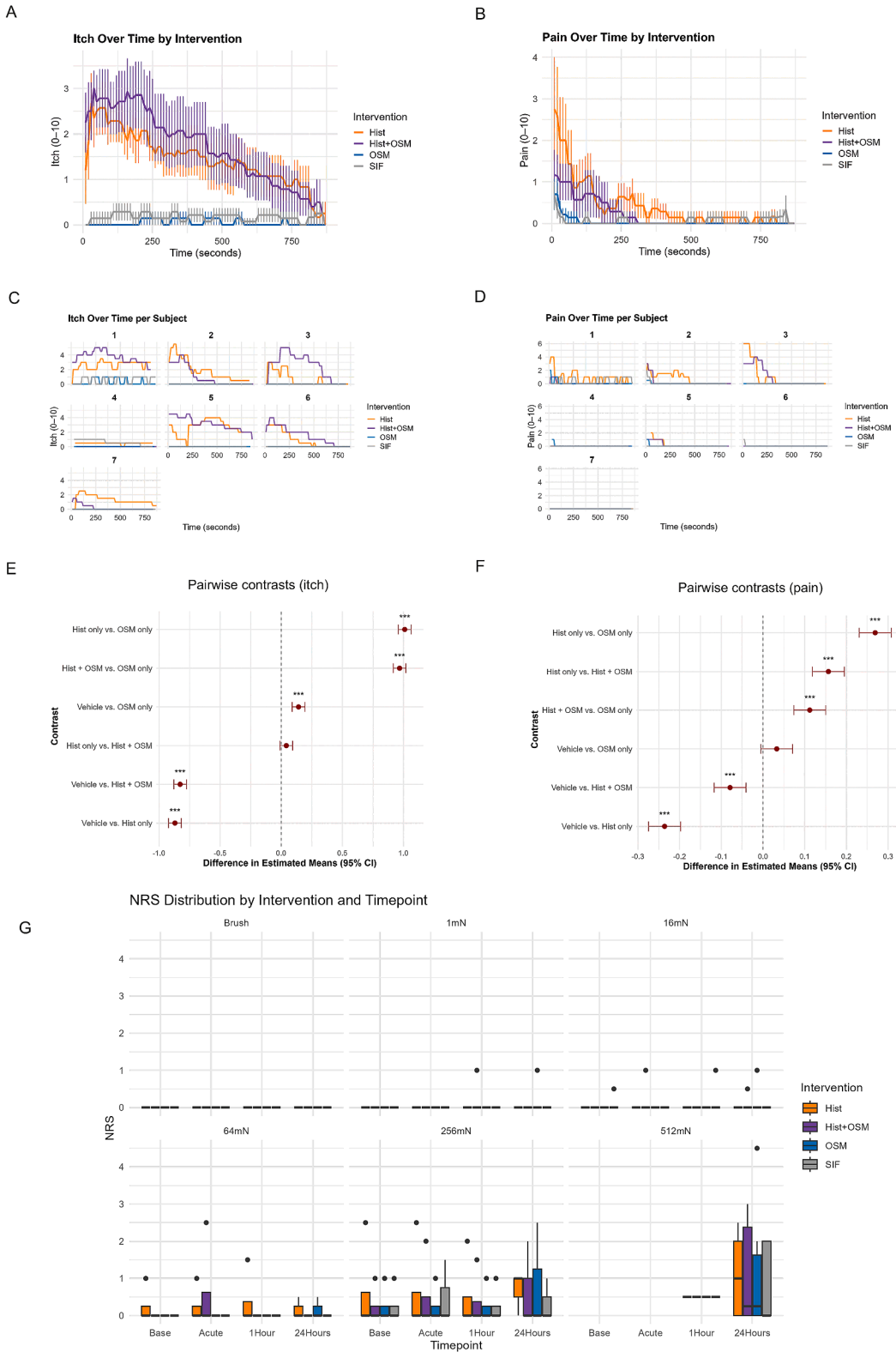

Figure S8. Effects of OSM, histamine, and their combination on itch and pain ratings over time, related to Figure 5

(A) Itch ratings over time (seconds) following intradermal injection of SIF (vehicle), histamine (Hist), OSM, or histamine + OSM (Hist + OSM) in seven subjects.

(B) Pain ratings over time for the same interventions and subjects.

(legend continued on next page)

(C and D) Individual subject itch (C) and pain (D) ratings plotted over time for each intervention condition.
(E) Pairwise model-based contrasts for itch ratings.
(F) Pairwise model-based contrasts for pain ratings.
(G) Mechanical pain ratings in response to von Frey hairs (1, 16, 64, 256, 512 mN) and brush stimulation at baseline, acutely post-injection, 1 and 24 h post-injection. $N = 7$ at all time points except 24 h, where $N = 6$. Statistical analyses were performed using linear mixed-effects models with fixed effects for intervention, time, and their interaction, and random intercepts for subjects. Model summaries and pairwise contrasts are provided in Tables S4 and S5.